J. Fluid Mech. (1991), *vol.* 226, *pp.* 445–474
Printed in Great Britain

Unsteady entrance flow in a 90° curved tube

By C. C. M. RINDT, A. A. VAN STEENHOVEN, J. D. JANSSEN AND G. VOSSERS

Departments of Mechanical Engineering and Physics, Eindhoven University of Technology,
Eindhoven, The Netherlands

(Received 9 February 1990 and in revised form 15 November 1990)

A numerical model enabling the prediction of the axial and secondary velocity fields in three-dimensional configurations at moderate Reynolds numbers and Womersley parameters is presented. Steady and unsteady entrance flows in a 90° curve tube ($\delta = \frac{1}{6}$) under various flow conditions are analysed. The good quality agreement between axial and secondary velocities for a sinusoidally varying flow rate at a Womersley parameter of $\alpha = 7.8$, obtained from a finite-element calculation, and those obtained from laser-Doppler measurements justify the use of the numerical model.

Halfway into the deceleration phase for a sinusoidally varying flow rate ($200 < Re < 800$, $\alpha = 7.8$) a strong resemblance is found to the steady flow case ($Re = 700$). In contrast with steady flow, near the inner wall reversed axial flow regions are found halfway into and at the end of the deceleration phase. Throughout the flow cycle the Dean-type secondary flow field highly influences axial flow resulting in a shift of the maximal axial velocity towards the outer wall, C-shaped axial isovelocity lines and an axial velocity plateau near the inner wall. Further downstream in the curved tube the Dean-type secondary vortex near the plane of symmetry is deflected towards the sidewall ('tail'-formation), as is also found for steady flow. An increase of the Womersley parameter ($\alpha = 24.7$) results in a constant secondary flow field which is probably mainly determined by the steady component of the flow rate. A study on the flow phenomena occurring for a physiologically varying flow rate suggests that the diastolic phase is only of minor importance for the flow phenomena occurring in the systolic phase. Elimination of the steady flow component ($-300 < Re < 300$) results in a pure Dean-type secondary flow field (no 'tail'-formation) for $\alpha = 7.8$ and in a Lyne-type secondary flow field for $\alpha = 24.7$. The magnitude of the secondary velocities for $\alpha = 24.7$ are of $O(10^{-2})$ as compared to the secondary velocities for $\alpha = 7.8$.

1. Introduction

Detailed analysis of unsteady entrance flow in a curved pipe is important for several reasons. First, fluid flow in a curved tube is of interest as a fundamental fluid-mechanical problem.Many investigators studied analytically fully developed flow in a curved pipe with a low curvature ratio (Dean 1927; Lyne 1970; Smith 1975). Only a few analytical studies, however, are performed on entrance flows in curved tubes (Singh, Sinha & Aggarwal 1978), owing to the complexity of the problem. Therefore, a numerical approach to the problem seems to be an appropriate way to gain more insight into the flow phenomena occurring in the entrance region of curved pipes. Secondly, this study was carried out in the context of a project studying the flow phenomena occurring in the carotid artery bifurcation. Olson (1971) studied steady flow in a symmetrical three-dimensional bifurcation using hot-wire anemometry, and compared the results with data obtained from velocity measurements performed in curved tubes. Olson concluded that the flow phenomena occurring in the daughter branches of such a symmetrical bifurcation are mainly determined by curvature effects. In spite of the fact that the geometry of the carotid artery bifurcation is highly asymmetric, the influence of curvature effects on the flow phenomena occurring in the daughter branches of this bifurcation are presumed to play an important role. Therefore, the entrance flow in a 90° curved tube was investigated to gain more insight into the complicated flow field in the carotid artery bifurcation.

In dimensionless form the Navier–Stokes and continuity equations are ruled by the Strouhal and Reynolds number, defined as $Sr = 2a\omega/U$ with ω a characteristic angular frequency, a the radius of the tube and U a characteristic velocity, and Re as $Re = 2aU/\nu$ with ν the kinematic viscosity. Unsteady fluid flow in a 90° curved tube is fully determined by these dimensionless quantities together with the geometry of the curved tube, characterized by the curvature ratio δ defined as $\delta = a/R$ with R the curvature radius of the axis of the tube. In analytical studies on fully developed fluid flows in curved tubes the Navier–Stokes and continuity equations are often presented in a toroidal coordinate system. It then appears that for loosely coiled pipes (low curvature ratios) the Dean number D ($D = Ga^3\delta^{\frac{1}{2}}/(\rho\nu^2)$ with G the mean axial pressure gradient and ρ the density), the Womersley parameter α ($\alpha = a(\omega/\nu)^{\frac{1}{2}}$) and the secondary Reynolds number R_s ($R_s = \delta U^2/(\nu\omega)$) are more appropriate to characterize fluid flow than the Reynolds number and the Strouhal number in combination with the curvature ratio. These numbers, in combination with the curvature ratio, are also commonly used for characterization of the flow phenomena occurring in curved tubes with higher curvature ratios. Because for entrance flows in curved tubes the mean axial pressure gradient G is not fixed, in studies on this subject the alternative Dean number κ is usually used, defined as $\kappa = \delta^{\frac{1}{2}}Re$. The secondary motions for fully developed flows in loosely coiled pipes are found to be governed by the secondary Reynolds number (Lyne 1970). In the present study we will focus mainly on the Reynolds number as a function of time and the Womersley parameter in combination with the curvature ratio. In the definition of the Reynolds number the instantaneous mean axial velocity is used as characteristic velocity. In the remainder of the text the alternative Dean number κ is mostly denoted as the Dean number.

Fully developed unsteady flows in curved tubes have been studied theoretically and/or experimentally by many investigators (Lyne 1970; Zalosh & Nelson 1973; Bertelsen 1975; Munson 1975; Smith 1975; Lin & Tarbell 1980; Mullin & Greated 1980; Berger, Talbot & Yao 1983). In recent studies on this subject (Chang & Tarbell 1985; Hamakiotes & Berger 1988) the system of equations was solved by a finite-difference method. Singh *et al.* (1978) performed an analytical study of unsteady entrance flow in a curved tube ($\delta = O(10^{-1})$) using a uniform inlet profile. Mullin & Greated (1980) used laser-Doppler anemometry for their velocity measurements in a curved tube with a curvature ratio of $\frac{1}{7}$. As the inlet condition an oscillating fully developed pipe flow was employed. The measurements were performed at a Womersley parameter of 0.99 and 4.36, while the peak Dean number ranged from 5.8 to 64.2. Chandran, Yearwood & Wieting (1979) performed laser-Doppler velocity measurements for a sinusoidally varying flow rate in a curved tube with a curvature ratio of $\frac{1}{10}$. The time-averaged Dean number was equal to 322 and the Womersley parameter was equal to 21.9. Chandran & Yearwood (1981) performed the same sort of study for a physiologically varying flow rate at a time-averaged Dean number of 320 and a Womersley parameter of 20.7. Talbot & Gong (1983) performed laser-Doppler experiments in a curved tube with a curvature ratio of $\frac{1}{20}$ and $\frac{1}{7}$. Two situations were investigated for which the characteristic flow parameters were $80 < \kappa < 160$, $\alpha = 8$ and $0 < \kappa < 744$, $\alpha = 12.5$, respectively. Perktold, Florian & Hilbert (1987) analysed pulsatile blood flow in a carotid siphon model, composed of several curved segments. They used the finite-element method to solve the time dependent, three-dimensional Navier–Stokes and continuity equations under physiological flow conditions.

The studies mentioned above dealing with unsteady entrance flows in curved tubes are either experimental or analytical/numerical. In none of these studies are experimental measurements confronted quantitatively with analytical or numerical calculations. In the present study on entrance flow problems of oscillating, pulsating and physiological flow rates in a 90° curved tube with a curvature ratio of $\delta = \frac{1}{6}$, both measurements and calculations are performed and a detailed comparison between the experimental and numerical results is carried out. In a study by van de Vosse *et al.* (1989), results are shown of a numerical and experimental study on steady entrance flow in a three-dimensional model of a 90° curved tube for Reynolds numbers up to 500. First, as a preparatory study, steady flow at a Reynolds number of 700 is investigated. A comparison of the calculated velocity field is made with that obtained from laser-Doppler velocity measurements of Bovendeerd *et al.* (1987). Next, the results of a velocity calculation are shown for a pulsating flow rate. The Reynolds number varied sinusoidally between 200 and 800, corresponding to the diastolic and systolic Reynolds numbers in the carotid artery bifurcation, respectively. The Womersley parameter was equal to 7.8, about twice the *in vivo* value. This value was chosen to match the sinusoidal flow rate variation with the physiological flow rate variation in the systolic phase of the heart cycle. For this particular case a detailed description of the axial and secondary flow fields is given as a function of time. To validate the numerical model, a detailed comparison with laser-Doppler velocity measurements is also made. Next, the influence of the frequency parameter on secondary flow is described. The results of a velocity calculation of fluid flow at a physiological flow rate are also shown, elucidating the influence of the waveform on the flow phenomena. Finally, the influence of the steady flow component is studied.

2. Methodology

2.1. *Numerical method*

For numerical modelling of incompressible, isothermal, laminar and Newtonian fluid flow in a 90° curved tube the Navier–Stokes and continuity equations have to be solved. In dimensionless form these equations read:

$$Sr\,\dot{\boldsymbol{u}}+\boldsymbol{u}\cdot\nabla\boldsymbol{u}-\frac{1}{Re}\Delta\boldsymbol{u}+\nabla p-\boldsymbol{f}=\boldsymbol{0}, \tag{1a}$$

$$\nabla\cdot\boldsymbol{u}=0, \tag{1b}$$

with $\boldsymbol{u}$ the velocity vector, p the pressure, $\boldsymbol{f}$ the body force per unit mass, ∇ the gradient vector operator and the superscript dot the local time derivative $\partial/\partial t$. To discretize these equations Galerkin's finite-element method was used, leading to the following set of ordinary differential equations (Cuvelier, Segal & Steenhoven 1986):

$$\boldsymbol{M}\dot{\boldsymbol{u}}+[\boldsymbol{S}+\boldsymbol{N}(\boldsymbol{u})]\boldsymbol{u}+\boldsymbol{L}^{\mathrm{T}}\boldsymbol{p}=\boldsymbol{f}+\boldsymbol{b}, \tag{2a}$$

$$\boldsymbol{L}\boldsymbol{u}=\boldsymbol{0}, \tag{2b}$$

where the column $\boldsymbol{u}$ contains the velocity unknowns (N) in the nodal points for the velocity and the column $\boldsymbol{p}$ the pressure unknowns (M) in the nodal points for the pressure. $\boldsymbol{M}$ is the mass matrix ($N \times N$), $\boldsymbol{S}$ the diffusion matrix ($N \times N$), $\boldsymbol{N}(\boldsymbol{u})$ the convection matrix ($N \times N$), $\boldsymbol{L}$ the divergence matrix ($M \times N$), $\boldsymbol{f}$ the body force column ($N \times 1$) and $\boldsymbol{b}$ the boundary stress column ($N \times 1$).

Elimination of the pressure unknowns from the discretized Navier–Stokes equation (2a) is performed by using the penalty function approach (Cuvelier *et al.* 1986). In discretized form the continuity equation reads:

$$\boldsymbol{L}\boldsymbol{u}=\epsilon\boldsymbol{M}_p\boldsymbol{p}, \tag{3}$$

with ϵ a very small parameter (the penalty parameter) and with $\boldsymbol{M}_p$ the pressure matrix ($M \times M$). If the right-hand side is small enough then the incompressibility of the fluid will be sufficiently approximated. It can be shown that for both the Stokes and Navier–Stokes equations, the solution of the penalty function approach converges to the solution of the unperturbed system for small values of the parameter ϵ (Pelissier 1975; Temam 1977).

The local time derivative is approximated by the θ-method. Consider a set of ordinary differential equations $\partial\boldsymbol{x}/\partial t=\boldsymbol{A}\boldsymbol{x}+\boldsymbol{r}$, then this finite-difference scheme reads (Cuvelier *et al.* 1986):

$$\begin{aligned}\frac{\boldsymbol{x}^{n+1}-\boldsymbol{x}^{n}}{\Delta t}&=(\boldsymbol{A}\boldsymbol{x}+\boldsymbol{r})^{n+\theta}\\&=\theta(\boldsymbol{A}\boldsymbol{x}^{n+1}+\boldsymbol{r}^{n+1})+(1-\theta)(\boldsymbol{A}\boldsymbol{x}^{n}+\boldsymbol{r}^{n}),\end{aligned} \tag{4}$$

in which $\boldsymbol{x}^n$ denotes $\boldsymbol{x}(n\Delta t)$ with Δt the timestep. The parameter θ can have values in the range $0 \leqslant \theta \leqslant 1$. For $\theta = 1$ this scheme reduces to the Euler-implicit scheme and for $\theta = 0$ to the Euler-explicit scheme, both $O(\Delta t)$ accurate in time. For $\theta = 0.5$ this scheme is known as the Crank–Nicolson scheme which is $O(\Delta t^2)$ accurate in time. Besides the accuracy of a finite-difference method, the stability of the scheme also has to be taken into account. Because an undamped behaviour is expected of numerical errors in the solution for the Crank–Nicolson scheme whereas for the Euler-implicit scheme these errors tend to zero, in many application fields a combination of these two methods is used (van de Vosse *et al.* 1986). First, several Euler-implicit timesteps are applied to damp numerical errors in the solution induced by the assumed initial condition. Secondly, the Crank–Nicolson scheme is applied to achieve a higher accuracy of the approximate solution.

Applying the penalty function approach and the θ-method to the discretized Navier–Stokes equation (equation (2a)) and linearization of the convective term by one step of a Newton–Raphson iteration scheme (Cuvelier *et al.* 1986) leads to:

$$[\boldsymbol{M}/\theta\Delta t+\boldsymbol{S}+\boldsymbol{J}(\boldsymbol{u}^n)+\frac{1}{\epsilon}\boldsymbol{L}^{\mathrm{T}}\boldsymbol{M}_p^{-1}\boldsymbol{L}]\,\boldsymbol{u}^{n+\theta}=[\boldsymbol{M}/\theta\Delta t+\boldsymbol{N}(\boldsymbol{u}^n)]\,\boldsymbol{u}^{n}+\boldsymbol{f}^{n+\theta}+\boldsymbol{b}^{n+\theta}, \tag{5}$$

with $\boldsymbol{J}(\boldsymbol{u})$ ($N \times N$) the Jacobian matrix of $\boldsymbol{N}(\boldsymbol{u})\boldsymbol{u}$. This is an Euler-implicit step from $\boldsymbol{u}^n$ to $\boldsymbol{u}^{n+\theta}$. The solution $\boldsymbol{u}^{n+1}$ is calculated afterwards from extrapolation of $\boldsymbol{u}^n$ and $\boldsymbol{u}^{n+\theta}$ to $\boldsymbol{u}^{n+1}$ using $\boldsymbol{u}^{n+\theta}=\theta\boldsymbol{u}^{n+1}+(1-\theta)\boldsymbol{u}^{n}$. Both schemes are in principal $O(\Delta t)$ accurate in time but a combination of these two methods, as described above, is similar to a Crank–Nicolson scheme which is $O(\Delta t^2)$ accurate in time (van de Vosse *et al.* 1986).

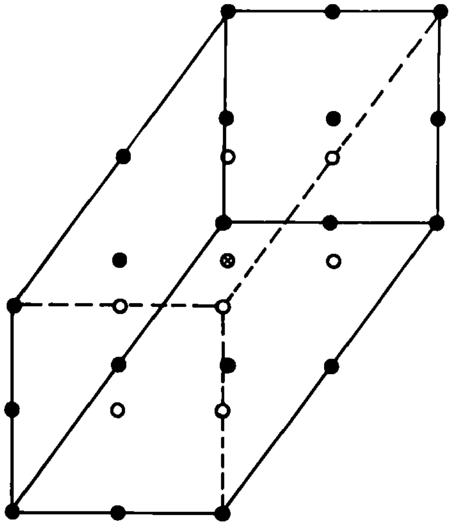

FIGURE 1. The 27-noded Crouzeix–Raviart element. ●, ○, u; ×, p, $\partial p/\partial x$.

The 27-noded element, as presented in figure 1, is used for division of the 90° curved tube into three-dimensional elements. Velocity unknowns are defined in all the nodal points of the element which means 81 velocity unknowns per element. The basis functions related to each nodal point are triquadratic functions. Pressure unknowns are only defined in the centre of the element, which are the pressure itself and its three spatial derivatives. The basis functions related to the pressure unknowns are a constant and three linear functions. Since these functions are zero outside the element under consideration, the pressure field varies discontinuously over the element boundaries. This type of element belongs to the group of the so-called Crouzeix–Raviart elements (Crouzeix & Raviart 1973). For this element the inverse of the pressure matrix (equation (5)) can be calculated elementwise (Cuvelier *et al.* 1986). Besides, the continuity equation is satisfied elementwise.

Discretization of the Navier–Stokes and continuity equations in combination with a penalty function approach leads to a system matrix with a symmetric profile structure. To economize the memory usage a profile storage technique was used. Previously performed calculations of steady entrance flow in a 90° curved tube (van de Vosse *et al.* 1989) revealed that large computing times (CPU-times) and input/output times (I/O-times) were needed for LU-decomposition of the system matrix resulting from a Galerkin finite element approach. Therefore, super and minisupercomputers were used in combination with a Sloan renumbering procedure (Sloan 1986) to reduce the bandwidth of the system matrix. In this study a minisupercomputer Alliant-fx/4 with 2 processors and a supercomputer Cyber-205 with 2 vectorpipes were used to solve the system of equations. To build and solve the system of equations and for presentation of the calculated results, the finite element package Sepran was used (Segal 1984).

Figure 2 shows the element division used for the reference flow case, which will be described below (sinusoidally varying flow rate: $200 < Re < 800$, $\alpha = 7.8$), consisting of 20 elements in the axial direction and 30 elements per cross-section. The lengths of the inlet and outlet sections are both 6 times the radius of the curved tube. Flow at the inlet was supposed to be fully developed and the velocities at the wall were

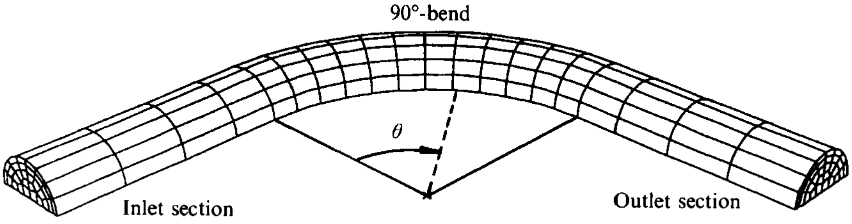

FIGURE 2. The element division for the 90° curved tube.

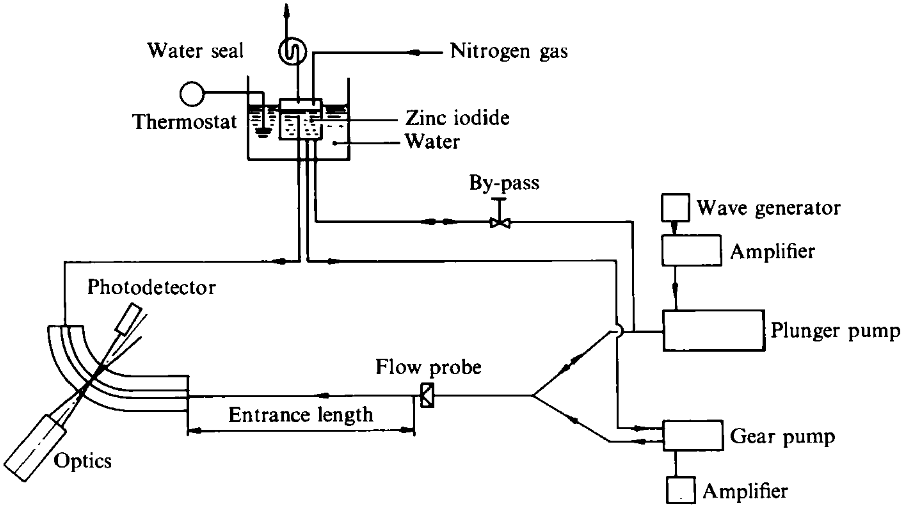

FIGURE 3. Fluid circuit for the unsteady flow experiments.

presumed to be zero, according to the no-slip condition. At the outlet the normal and both tangential stresses were set to zero, while in the plane of symmetry both tangential stresses and the normal velocity component were put to zero.

From velocity calculations in a two-dimensional model of the carotid artery bifurcation (Rindt *et al.* 1987), it appeared that 20 timesteps per period were sufficient to achieve an accurate solution. For the reference flow case one period consisted of 24 timesteps. A zero velocity field was used as the initial condition. To damp numerical errors induced by this initial condition, an Euler-implicit time integration scheme was first applied for $\frac{3}{4}$ of a period. Hereafter, a Crank–Nicolson time integration scheme was employed until the maximal difference between the velocity components of the solution at the same time intervals of two successive periods was smaller than 10^{-2} times the mean axial velocity. For the reference flow case, 3 periods were needed to reach this goal.

2.2. *Experimental method*

The velocity measurements to validate the numerical model were performed with a one-component forward-scattering reference-beam laser-Doppler anemometer. Drain (1981) gives an extensive description of the physical aspects of this method. In figure 3 a schematic presentation of the fluid circuit used is given. A gear pump was used for generation of the steady flow component (Verder) and the unsteady flow component was generated by a piston-in-cylinder pump driven by a programmable

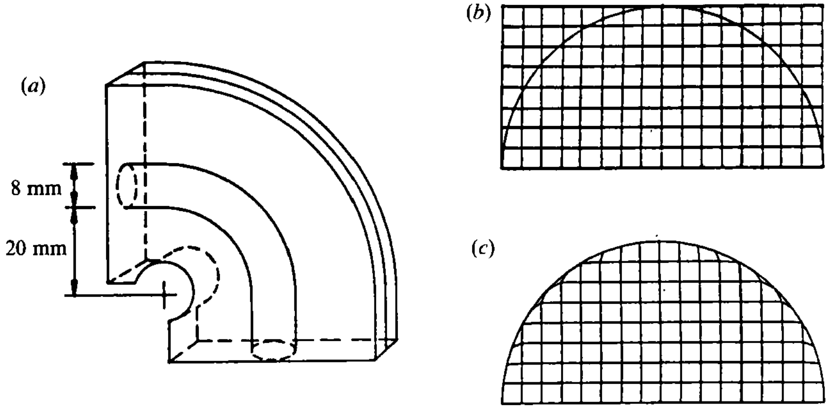

FIGURE 4. (*a*) The Perspex model of the 90° curved tube, (*b*) the measuring grid and (*c*) the finite element mesh.

waveform generator (Vivitro Systems Incorporated). The waveform generator also provides an output signal to facilitate synchronization to external instrumentation. As connecting tubes between the various systems, wire-reinforced tubes were used to avoid wave propagation and reflection phenomena. An entrance length of 50 tube diameters was used to ensure that fluid flow was fully developed before it reached the measuring section. The three-dimensional model consisted of two halves of Perspex, split at the plane of symmetry, in which the 90° curved tube was machined out (figure 4*a*). The curvature ratio of the 90° curved tube was equal to $\delta = \frac{1}{6}$. A solution of zinc iodide was used as the measuring fluid, enabling exact matching of the refraction index to the one of Perspex. Because a zinc iodide solution is somewhat poisonous and rather aggressive, it must be treated with care. Also, high internal stresses in the Perspex model should be avoided because otherwise cracks may occur.

Data were measured by a system controlled by a personal computer. Fifty samples were taken per period. The start of data intake was controlled by a trigger pulse. This trigger pulse was generated by the wave generator of the plunger pump. After calibration of the measuring system and the laser-Doppler equipment, the data obtained were converted to physical units. Beside the mean values, 95%-confidence intervals based on a Student-*t* distribution were calculated. Therefore, 10 periods were measured.

For measurement of the axial velocity component and the secondary velocity component parallel to the plane of symmetry, the optical axis of the He–Ne laser was put perpendicular to the plane of symmetry of the three-dimensional model used. By rotation of the plane spanned by the laser beams both velocity components could be obtained. For measurement of the secondary velocity component perpendicular to the plane of symmetry the optical axis had to be parallel and the plane spanned by the laser beams had to be perpendicular to the plane of symmetry. The problem with this kind of measurement is that total reflection at the plane of symmetry may occur to one of the laser beams, owing to an air film between the two halves of Perspex. Therefore, a Perspex model was used which was split along the axis of the tube and perpendicular to the plane of symmetry.

Three stepper motors were used to traverse the model in three independent directions, through which positioning of the measuring volume at various sites in the model was possible. Owing to the step size, positioning of the measuring volume occurred with an accuracy of $\pm 3\,\mu$m, $\pm 8\,\mu$m and $\pm 8\,\mu$m in the x-, y- and z-

directions, respectively. Detailed analysis of the axial and secondary velocity distributions was performed at 5 levels in the 90° curved tube. At each level the measuring volume was traversed according to a rectangular grid (figure 4*b*). Independently, the axial velocity component and both secondary velocity components were measured in each grid point. Afterwards, for presentation purposes, the rectangular measuring grid was transformed to a finite element mesh (figure 4*c*). The velocities at the wall were presumed to be zero according to the no-slip boundary condition. Then, using post-processing software, axial and secondary flow fields were presented by axial isovelocity lines and secondary velocity vectors, respectively.

Several kinds of error sources result in detection errors of the fluid velocities. First, errors result from small variations in the fluid velocity owing to small variations in the imposed flow rate and the limited electronic detection accuracy of the frequency of the photodetector signal. Also frequency instabilities of the plunger pump result in detection errors. All these errors can be estimated by calculation of the 95%-confidence intervals, which were found to be less than 1% of the maximal axial velocity.

Errors also result from positioning failures of the measuring volume owing to localization errors of a starting point and the finite accuracy of the traversing system. Detection errors of the velocity caused by these positioning errors are estimated to be 5% of the local velocity. Also, errors are caused by failures in the adjustment of the correct angles, resulting in the measurement of the wrong velocity component. The largest absolute errors occur in the detection of the secondary flow field, which are estimated to be 2% of the local axial velocity. However, in regions with low axial velocities, large relative errors in the detection of axial velocities may occur owing to the secondary velocity components. Next, errors in the determination of the angle between the reference and the main beam cause detection errors of the velocity, which are estimated to be $\pm 0.5\%$. The large size of the measuring volume ($400\ \mu m \times 40\ \mu m \times 40\ \mu m$) with regard to the size of the three-dimensional models used (8 mm), also causes detection errors of the velocity, dependent on the velocity gradients. The highest influence of these errors is expected near the sidewalls of the models, where the velocity gradients are mostly large. The largest errors are expected for the secondary velocity component parallel to the plane of symmetry because for this component the largest dimension of the measuring volume was positioned in the direction of the largest velocity gradients near the sidewall. The resulting errors in that case can be up to 20% of the maximal secondary velocity. Finally, errors result from adjustment failures of the correct Reynolds number and Womersley parameter. Errors in the Reynolds number are caused by inaccuracies in the values of the flow rate and the kinematic viscosity and are estimated to be $\pm 5\%$ of the mean Reynolds number. It is remarked that a small deviation in Reynolds number may cause a considerable shift in the axial isovelocity lines, especially where small velocity gradients are present. Finally, errors in the adjustment of the Womersley parameter are estimated to be $\pm 1\%$.

3. Steady entrance flow

3.1. *Introduction*

In a study performed by van de Vosse *et al.* (1989) the results of finite element calculations of steady flow in a 90° curved tube with a curvature ratio of $\frac{1}{6}$ are presented for Reynolds numbers up to 500. Application of higher Reynolds numbers caused oscillations in the predicted velocity field, probably owing to bifurcation of

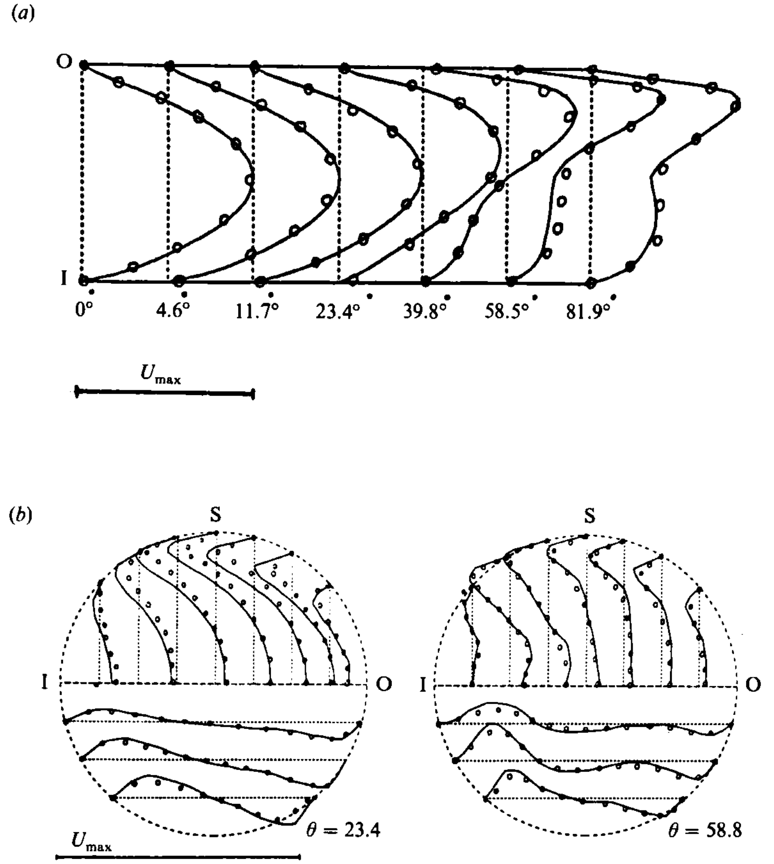

FIGURE 5. (*a*) Calculated (—) and measured (○) axial velocity profiles in the plane of symmetry (I, inner wall; outer wall). (*b*) Calculated (—) and measured (○) secondary velocity profiles (I, inner wall; O, outer wall; S, sidewall).

the solution in this range of Reynolds numbers or to a too coarse element division. To avoid these problems, in this study a finer element division is employed and iteration towards a Reynolds number of 700 was achieved by first solving the unsteady and then solving the steady Navier–Stokes problem. The maximal difference between the velocity components of the final 2 iterations was smaller than 10^{-6} times the mean axial velocity. For the steady flow case the same element division was used as depicted in figure 2. Also the boundary conditions were the same as already described for the reference flow case except for the ones at the inlet. There, flow was supposed to be fully developed, which means a parabolic axial flow field and zero secondary velocities.

3.2. *Comparison with experiments*

Bovendeerd *et al.* (1987) performed an experimental study of steady entrance flow in a 90° curved tube, with a curvature ratio of $\frac{1}{6}$, at a Reynolds number of 700. A laser-Doppler anemometer was used to measure axial and secondary velocities at 7 positions in the curved tube ($\theta = 0°$, 4.6°, 11.7°, 23.4°, 39.8°, 58.8° and 81.9°). See Bovendeerd *et al.* (1987) for a detailed description of axial and secondary flow. In short, owing to centrifugal forces a secondary flow develops which is directed from the inner wall towards the outer wall near the plane of symmetry and circumferentially back near the sidewall, resembling a Dean-type vortex. This secondary motion results in a shift of the maximal axial velocity towards the outer wall on the one hand and an injection of fluid particles with high axial velocities near the sidewall on the other, resulting in C-shaped axial velocity contours. Further downstream in the curved tube, 'tail'-formation (deflection of the Dean-type vortex towards the sidewall) in the secondary flow field takes place near the centre of the curved tube.

A comparison with the measurements of Bovendeerd *et al.* (1987) is performed by comparing the axial velocity profiles in the plane of symmetry. In figure 5(*a*) these axial velocity profiles are presented for both the measurements and the calculations. There is a good agreement between the experimental and numerical data. In the numerical case the axial velocity plateau at $\theta = 58.5°$ is somewhat less developed. For a comparison between the calculated and measured secondary flow field, in figure 5(*b*) secondary flow at $\theta = 23.4°$ and 58.5° is presented by velocity profiles of the component parallel to the plane of symmetry (upper half) and the component perpendicular to the plane of symmetry (lower half). Here again relatively good agreement exists between the experimental and numerical results. The largest differences are found near the sidewall at $\theta = 23.4°$, where the calculated secondary velocities parallel to the plane of symmetry are higher than the measured ones. Probably, measuring errors due to positioning of the largest dimension of the measuring volume in the direction of the steepest velocity gradients contribute to this discrepancy.

4. Unsteady entrance flow

4.1. *Introduction*

In this section a detailed description of unsteady entrance flow in a 90° curved tube at a particular set of parameters is given. To validate the numerical model both axial and secondary flow are compared with experimental results. The flow rate consisted of a sinusoidally varying unsteady flow component ($-300 < Re < 300$) superimposed on a steady flow component ($Re = 500$). With a curvature ratio of $\frac{1}{6}$ this yields a Dean number varying between 82 and 327. The Womersley parameter was equal to 7.8. In the remainder of the text this flow case will be denoted as the reference flow case or flow case 1. The element division used and the boundary condition prescribed, are already reported in the description of the numerical method. The time intervals at which the results are reported corresponds to mean flow rate in the acceleration phase ($t = 0$), to maximal flow rate ($t = \frac{1}{4}T$), to mean flow rate in the deceleration phase ($t = \frac{1}{2}T$) and to minimal flow rate ($t = \frac{3}{4}T$).

4.2. *Description of the flow field*

In figure 6 the results of axial and secondary flow at 5 axial positions in the curved tube ($\theta = 0°$, 22.5°, 45°, 67.5° and 90°) are shown. Axial flow is presented by axial isovelocity lines and secondary flow is visualized by means of velocity vectors. Contour level 0 corresponds to zero axial velocity and the difference in axial velocity between two successive levels is equal to 0.32 times the mean axial velocity at $t = 0$ (U_{mn}). The secondary velocities at $\theta = 0°$ are scaled up three times, as compared to the secondary velocities at the other cross-sectional planes.

At $\theta = 0°$ (figure 6*a*) the axial velocity contours at $t = \frac{1}{2}T$ and $\frac{3}{4}T$ are almost concentric circles. At $t = 0$ and $\frac{1}{4}T$ the maximum of axial velocity is slightly shifted towards the inner bend of the curved tube, resulting in larger axial velocity gradients

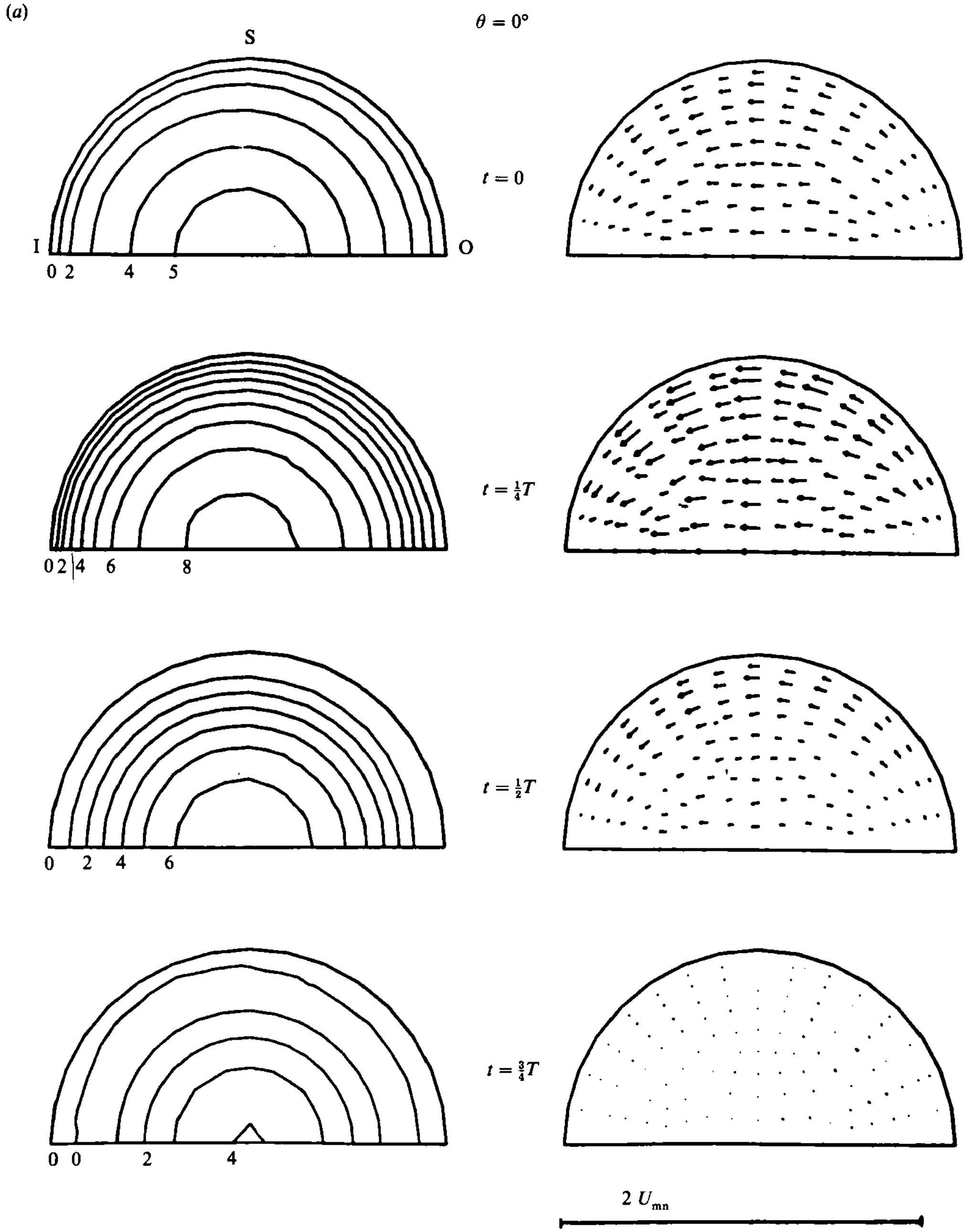

FIGURE 6(*a*). For caption see page 459.

at the inner wall, as compared to those at the outer wall. The secondary velocities are completely directed from the outer wall towards the inner wall, pointing at upstream influences of the curved tube. These secondary velocities are about equal halfway into the acceleration and deceleration phases. They are almost zero at minimal flow rate. At maximal flow rate, oscillations are observed in the secondary flow field, possibly owing to numerical failures as a consequence of a too coarse element division in the axial direction or a too short entrance length. A calculation of the velocity field

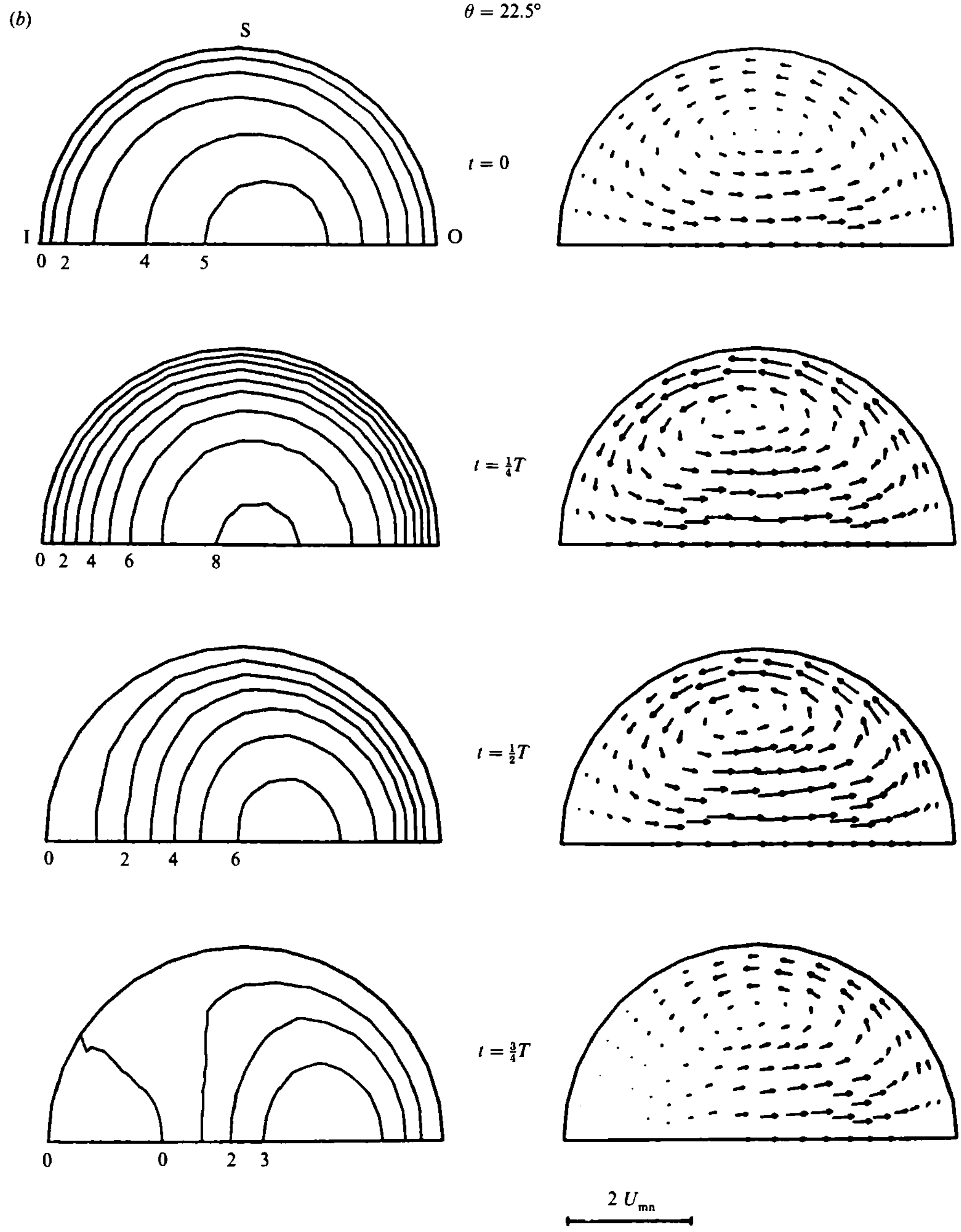

FIGURE 6(b). For caption see page 459.

in a curved tube with a smaller entrance length and larger elements showed larger oscillations in the secondary flow field. The solution further downstream in the curved tube, however, was not affected.

At $\theta = 22.5°$ (figure 6b) the secondary velocities near the plane of symmetry are directed towards the outer bend, as a consequence of centrifugal forces, whereas near the sidewall of the curved tube these secondary velocities are directed towards the inner bend, resulting in a Dean-type secondary flow field. For the total period of time the centre of this secondary vortex is situated near the centreline of the cross-

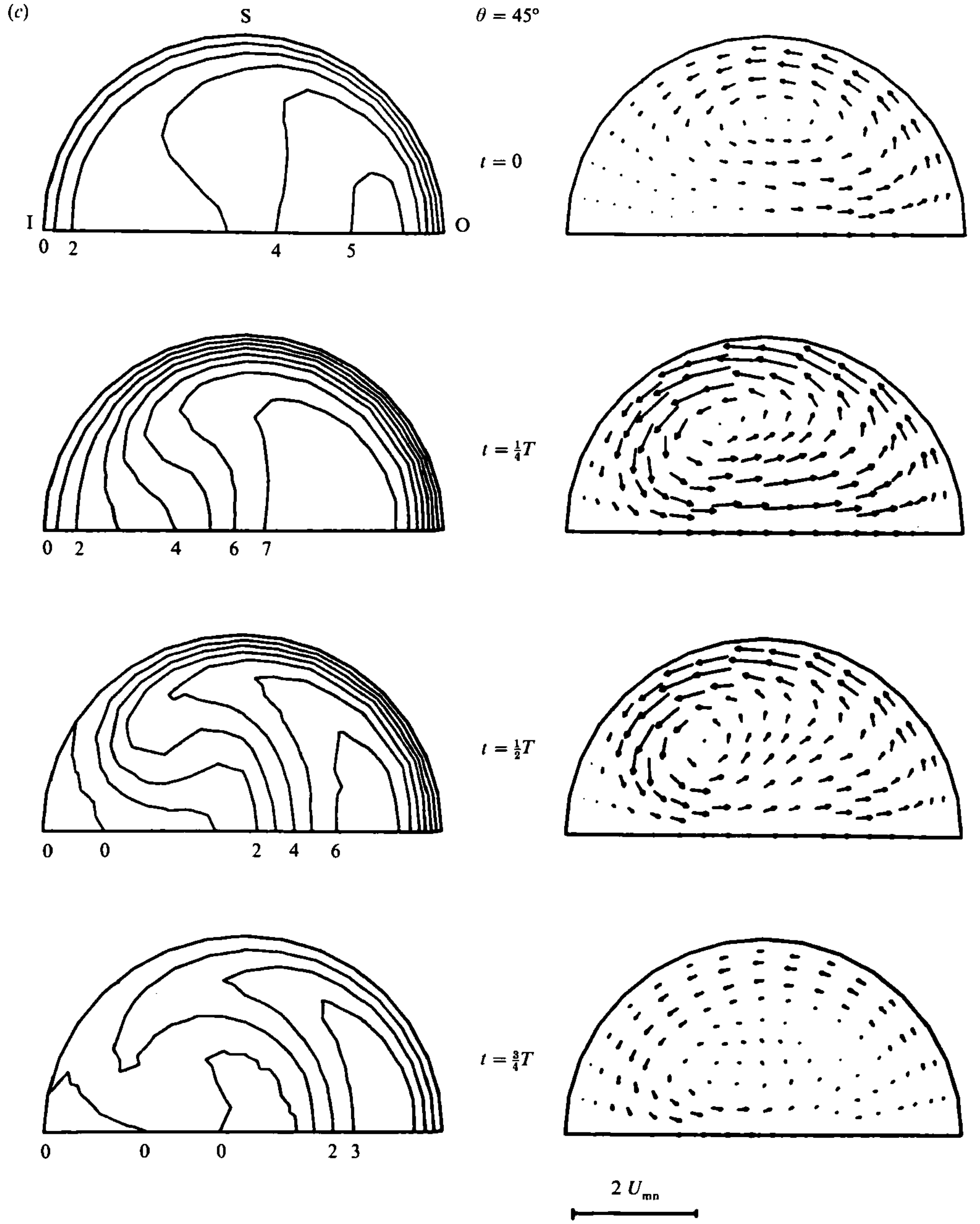

FIGURE 6(*c*). For caption see page 459.

sectional plane. The secondary velocities at $t = \frac{1}{4}T$ and $\frac{1}{2}T$ are about equal, as well as the secondary velocities at $t = \frac{3}{4}T$ and $t = 0$. At minimal flow rate a region with low secondary velocities is found near the inner bend. As a consequence of secondary flow a shift of the maximum of axial velocity towards the outer bend is observed for the whole period of time. This shift is maximal at minimal flow rate ($t = \frac{3}{4}T$). At this time interval a region with negative axial velocities is observed at the inner bend. The largest axial velocity gradients are found at the outer wall at maximal flow rate ($t = \frac{1}{4}T$).

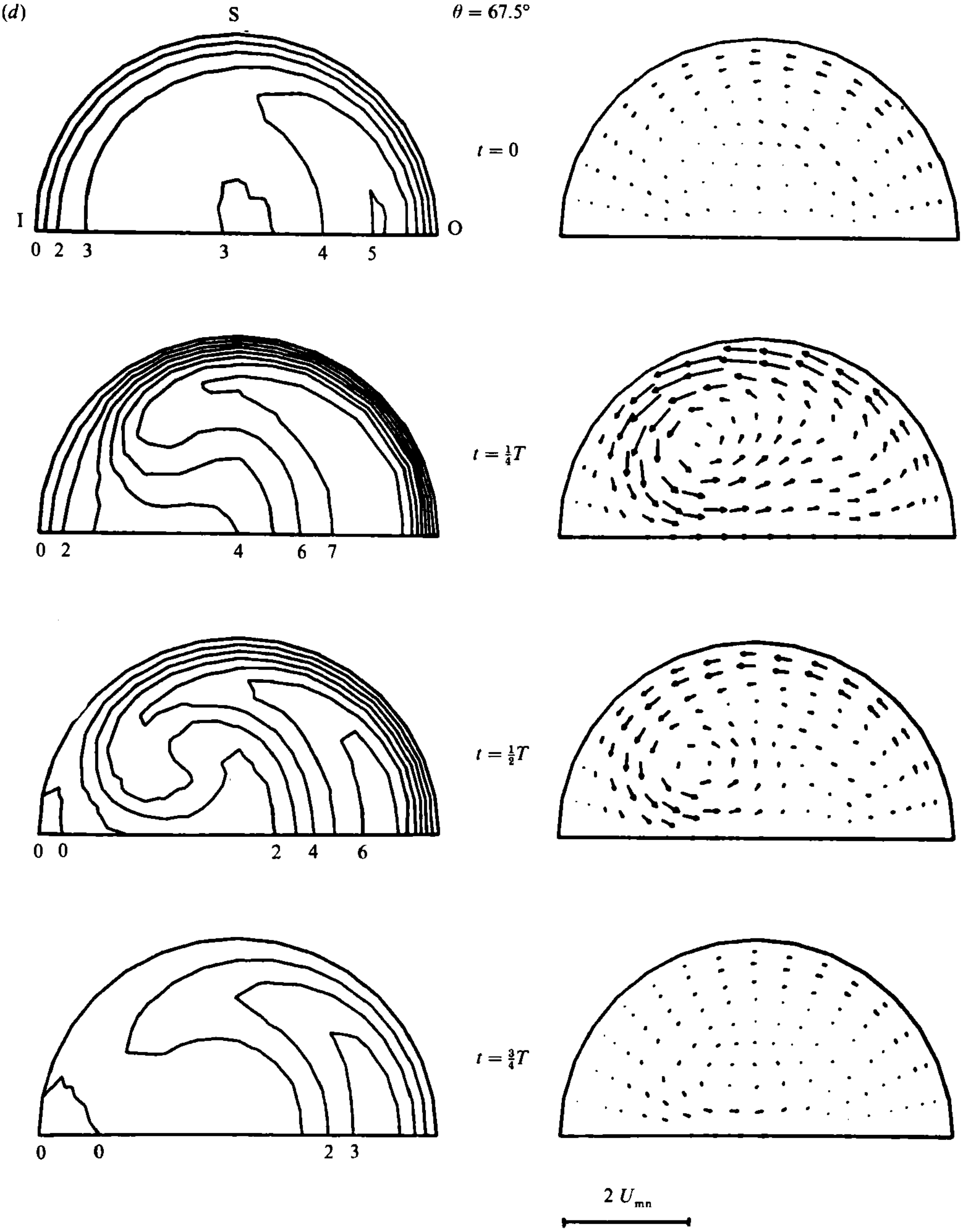

FIGURE 6(*d*). For caption see facing page.

The highest secondary velocities throughout the curved tube occur at $\theta = 45°$ (figure 6*c*) at peak flow rate. Still, the secondary velocities are directed from the inner wall towards the outer wall near the plane of symmetry and circumferentially back near the sidewall. The centre of the vortex is situated near the centre line of the cross-sectional plane for $t = 0$ and it is slightly shifted towards the inner wall for $t = \frac{1}{4}T$, $\frac{1}{2}T$ and $\frac{3}{4}T$, describing some kind of circle. In the deceleration phase and at minimal flow rate a 'tail' in the secondary flow field develops, through which the secondary velocities in the central region of the tube are no longer parallel to the plane of

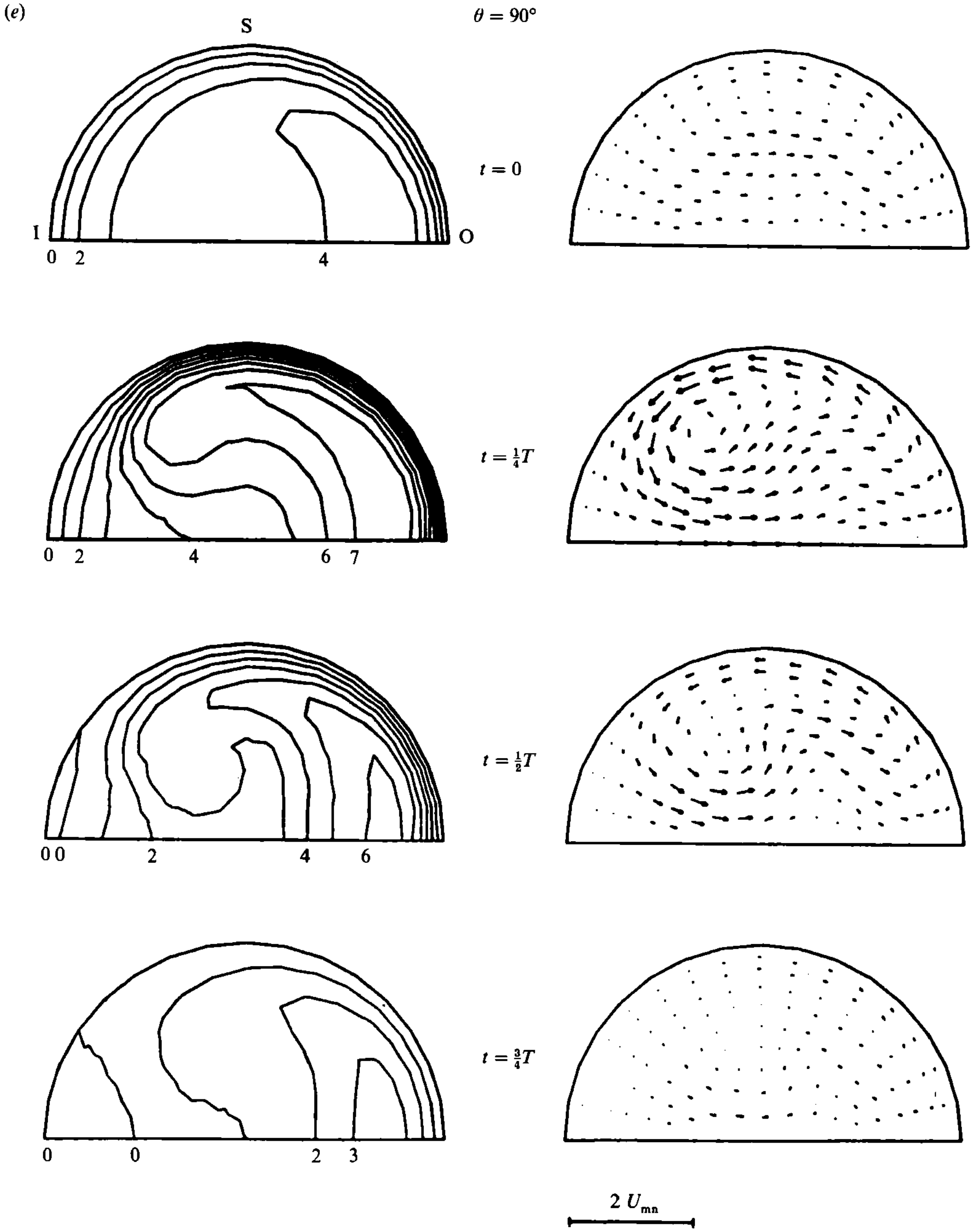

FIGURE 6. Axial and secondary flow for the reference flow case (I, inner wall; O, outer wall; S, sidewall; U_{mn}, time-averaged mean axial velocity). (*a*) $\theta = 0°$, (*b*) $\theta = 22.5°$, (*c*) $\theta = 45°$, (*d*) $\theta = 67.5°$, (*e*) $\theta = 90°$.

symmetry but slightly directed towards the sidewall. Possibly, this 'tail'-formation is due to the relatively large axial velocity gradients in the central region. The shift of the axial isovelocity lines towards the outer wall continues, as compared to the shift at $\theta = 22.5°$, resulting in large axial velocity gradients at the outer wall. The largest shift is found at $t = \frac{3}{4}T$ but, owing to the smallest flow rate at this time interval, the axial velocity gradients are relatively small. At all time intervals C-

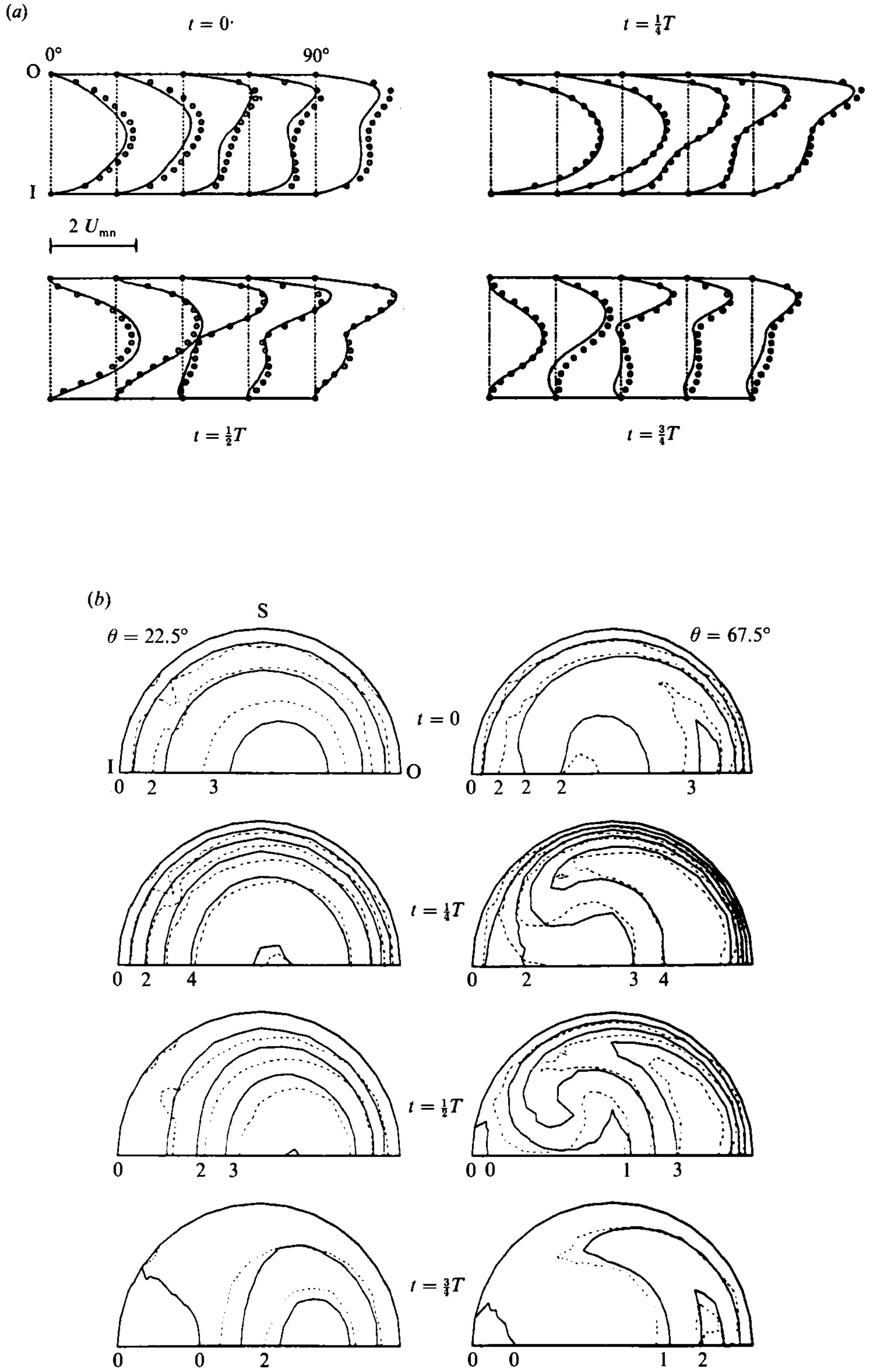

FIGURE 7 (a, b). For caption see facing page.

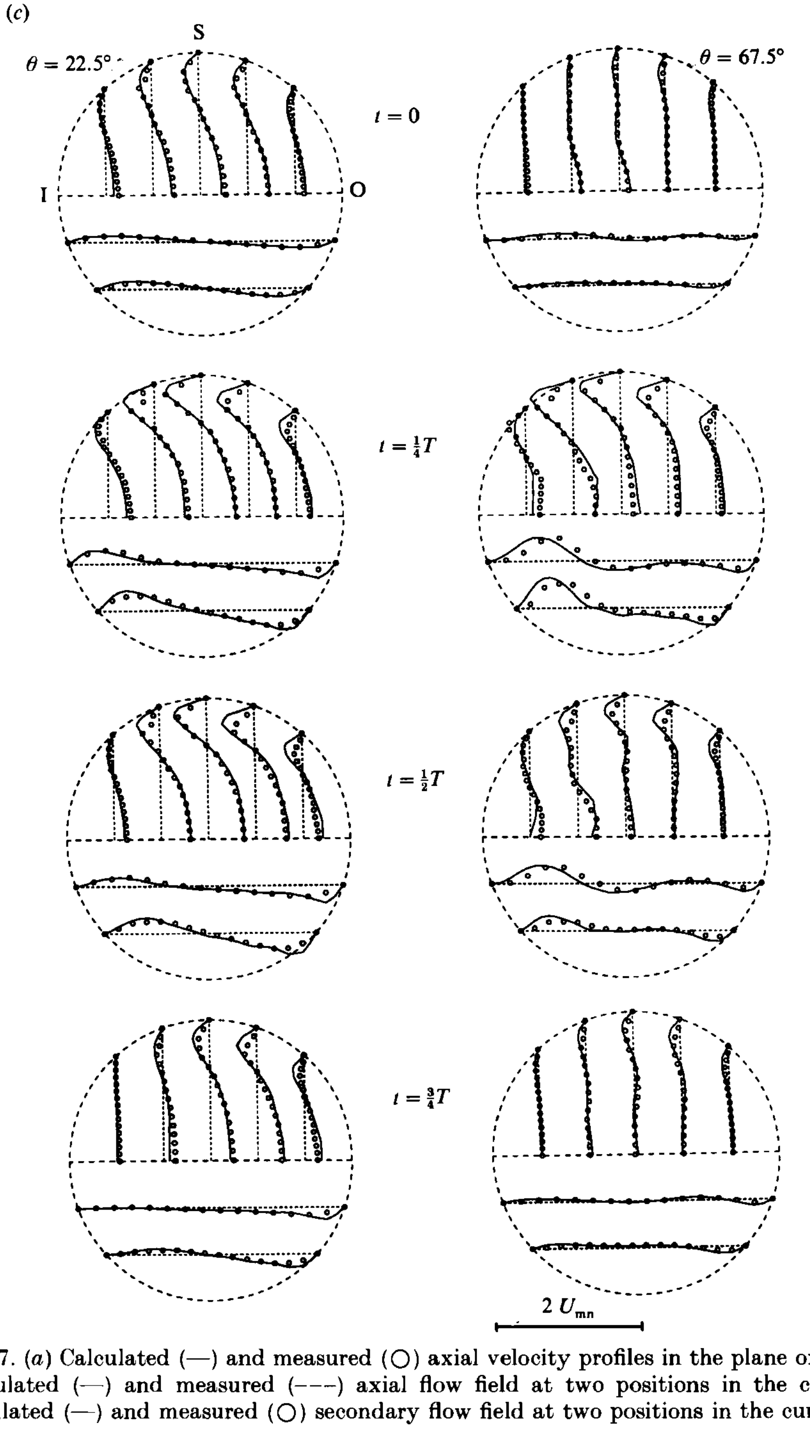

FIGURE 7. (*a*) Calculated (—) and measured (○) axial velocity profiles in the plane of symmetry. (*b*) Calculated (—) and measured (---) axial flow field at two positions in the curved tube. (*c*) Calculated (—) and measured (○) secondary flow field at two positions in the curved tube.

shaped axial velocity contours are observed, which develop in the deceleration phase and become less pronounced in the acceleration phase. These C-shaped axial velocity contours are caused by secondary flow, through which fluid particles with high axial velocities situated at the outer bend are injected at the inner bend. Halfway into the deceleration phase, at $t = \frac{1}{2}T$, a region with negative axial velocities is observed near the inner wall. Also at minimal flow rate ($t = \frac{3}{4}T$) a region with reversed axial flow is found in the central region of the tube. At $t = 0$ large regions occur with hardly varying axial velocities, pointing to the formation of axial velocity plateaus.

At $\theta = 67.5°$ (figure 6*d*) the secondary velocities are considerably lower, as compared to the secondary velocities halfway into the curved tube, except at maximal flow rate ($t = \frac{1}{4}T$). At $\theta = 67.5°$ the 'tail' in the secondary flow field is also observed at maximal flow rate and it intensifies in the deceleration phase. The position of the centre of the secondary vortex at $t = \frac{1}{4}T$, $\frac{1}{2}T$ and $\frac{3}{4}T$ is almost the same as compared to the position halfway into the curved tube. Also in the deceleration phase, C-shaped axial velocity contours develop with highly curved segments at $t = \frac{1}{2}T$. Halfway into the acceleration phase ($t = 0$) a local minimum is observed at the centre of the tube. Regions with almost constant axial velocities occur at minimal flow rate ($t = \frac{3}{4}T$) and halfway into the acceleration phase ($t = 0$). Reversed axial flow regions are found near the inner wall at $t = \frac{1}{2}T$ and $\frac{3}{4}T$. The region with negative axial velocities at the centre of the tube has disappeared.

All in all, the axial and secondary flow fields at $\theta = 90°$ (figure 6*e*) have the same appearance as the flow fields at $\theta = 67.5°$. The secondary velocities at maximal flow rate, however, are lower, as compared with the secondary velocities at $\theta = 67.5°$. Also the C-shaped axial velocity contours are less pronounced at $t = \frac{3}{4}T$ and the local axial velocity minimum at $t = 0$ has disappeared.

4.3. *Comparison with experiments*

To validate the numerical results, laser-Doppler experiments were performed in a 90° curved tube. Although the adjusted flow rate in the experiments consisted of a sinusoidally varying component ($-300 < Re < 300$) superimposed on a steady flow component ($Re = 500$), some differences with the numerical situation were found to be present. It appeared that the minimal Reynolds number was 250 instead of 200 and that the Reynolds numbers halfway into the acceleration ($t = 0$) and deceleration phase ($t = \frac{1}{2}T$) were, respectively, 565 and 460. Errors in the calculation of these Reynolds numbers resulting from numerical integration of the axial flow field are estimated to be ± 10. The rather large differences between the experimental and numerical situation can possibly be explained by the strategy applied for the adjustment of the flow rate in the experiments. First, the steady flow component was adjusted at a Reynolds number of 500. Afterwards the unsteady flow component was imposed and a maximal Reynolds number of 800 was adjusted. In this strategy, however, the influence of the unsteady flow component on the 'steady' flow component was not taken into account, which may result in the observed discrepancies. Besides, the sampling frequency of 50 samples per period contributes to these discrepancies. Owing to this sampling frequency, data presentation at exactly minimal, mean and maximal flow rate is impossible. This may result in errors in the Reynolds number of ± 20 at mean flow rate. Despite these experimental deviations, the measurements seem to be appropriate to validate qualitatively the numerical model used.

A comparison with the laser-Doppler velocity measurements is achieved by presentation of the axial velocities in the plane of symmetry and the axial contour levels and secondary velocity profiles at $\theta = 22.5°$ and $67.5°$. In figure 7(*a*) the axial velocity profiles in the plane of symmetry are presented as a function of time for both the measurements and the calculations. A good agreement between the experimental and numerical data is observed. The largest differences occur halfway into the acceleration phase at $t = 0$ and at the end of the deceleration phase at $t = \frac{3}{4}T$. For both time intervals the velocities found in the experiments are somewhat higher than the velocities calculated by the numerical model, probably caused by the larger Reynolds number in the experiments at these time intervals. For the experiments this discrepancy results in the absence of regions with reversed axial flow downstream in the curved tube at minimal flow rate ($t = \frac{3}{4}T$). The shift of the maximum of axial velocity towards the outer wall is clearly seen at all time intervals. Also the presence of a local minimum in the axial velocity field at $\theta = 67.5°$ and $t = 0$ is observed for both the measurements and the calculations. Such minima also occur downstream in the curved tube at $t = \frac{1}{2}T$ and $\frac{3}{4}T$.

In figure 7(*b*) the axial velocity contours at $\theta = 22.5°$ and 67.5° are presented as function of time. Contour level 0 corresponds to zero axial velocity and the difference in axial velocity between two successive levels corresponds to 0.52 times the time-averaged mean axial velocity (U_{mn}). The agreement between the numerical and experimental data is satisfactory. The regions with reversed axial flow calculated by the numerical model at the end of the deceleration phase are absent in the experiments, probably owing to the larger Reynolds number in the experiments at this time interval. The largest differences in the C-shaped appearance of the axial velocity contours occur at $\theta = 67.5°$ and $t = \frac{1}{2}T$, where the curvature of the contour levels 2 and 3 is more pronounced, whereas the curvature of contour level 1 is less pronounced for the computations, possibly also as a consequence of the difference in the Reynolds number at this time interval. The position of the local axial velocity minimum at $\theta = 67.5°$ and $t = 0$ is closer to the inner bend for the experiments than for the calculations.

A comparison of the secondary flow field is performed with the use of velocity profiles of secondary flow. In figure 7(*c*) the component of secondary flow parallel to the plane of symmetry is presented in the upper half and the component perpendicular to the plane of symmetry in the lower half of the cross-sectional area. The agreement between the experimental and numerical data is fair. The largest differences occur in the component parallel to the plane of symmetry near the sidewall of the curved tube at both positions for $t = \frac{1}{4}T$ and $\frac{1}{2}T$. Near the plane of symmetry the largest differences in this component occur at $\theta = 67.5°$ for $t = \frac{1}{4}T$ and $\frac{1}{2}T$, but these differences are small compared to the differences near the sidewall. Possibly, the rather large dimensions of the measuring volume contribute to these discrepancies. The main differences in the component perpendicular to the plane of symmetry occur at $\theta = 67.5°$ for $t = \frac{1}{4}T$and $\frac{1}{2}T$, where a shift in the profiles near the inner bend of the curved tube is observed, probably owing to positioning errors of the measuring volume.

5. Influence of various parameters on axial and secondary flow

5.1. *Introduction*

To gain more insight into the influence of the frequency parameter and the steady flow component on axial and secondary flow, calculations were performed at a Womersley parameter of 15 and 24.7, for a Reynolds number varying between 200 and 800, and at a Womersley parameter of 7.8 and 24.7, for a Reynolds number varying between −300 and 300. For the latter two flow cases the Reynolds number was adjusted by lowering the axial velocity values. Also axial and secondary flow were investigated for a physiologically varying flow rate, as presented in figure 8. The Reynolds number varied between 200 and 800, with a time-averaged mean Reynolds

	Reynolds number	Dean number	Womersley parameter	Flow wave
Case 1	200:800	82:327	7.8	pulsating
Case 2	200:800	82:327	15.0	pulsating
Case 3	200:800	82:327	24.7	pulsating
Case 4	200:800	82:327	4.0	physiological
Case 5	−300:300	−122:122	7.8	oscillating
Case 6	−300:300	−122:122	24.7	oscillating

TABLE 1. Summary of the parameters for the unsteady flow cases

	N_{cross}	N_{axial}	N_{in}	N_{out}	L_{in}	L_{out}	N_{conv}
Case 1	30	20	4	4	6	6	3
Case 2	30	15	1	2	2	2	6
Case 3	30	15	1	2	2	2	9
Case 4	30	20	4	4	6	6	1.5
Case 5	20	28	8	8	20	20	6
Case 6	30	20	4	4	6	6	3

TABLE 2. Details of the element divisions used (N_{cross}, N_{axial}, N_{in} and N_{out} correspond, respectively, to number of elements per cross-section, in axial direction, in inlet section and in outlet section, L_{in} and L_{out} correspond to lengths of inlet and outlet section) and number of periods needed to reach convergence (N_{conv}) for the various flow cases

number of about 300. The Womersley parameter for this flow case was equal to 4. All the parameters, including the Dean number, for the different flow cases studied, are summarized in table 1.

In Table 2 details of the element divisions used are given, like the number of elements per cross-section, the number of elements in the axial direction, the lengths of the inlet and outlet sections and so forth. For the flow cases 2 and 3 the element division consisted of 15 elements in the axial direction and 30 elements per cross-section. The lengths of the inlet and outlet sections were equal to twice the radius of the tube and consisted of 1 and 2 elements in the axial direction, respectively. Using this element division for the calculation of axial and secondary flow for flow case 1, no remarkable differences with the results presented earlier were found. For flow case 4 the same element division was used as for flow case 1. The boundary conditions for flow cases 2, 3 and 4 were the same as employed for flow case 1, i.e. at the inlet fully developed unsteady pipe flow was assumed. To that end, for the physiological flow wave 15 harmonics were used to correctly prescribe the axial flow field at the inlet. From a velocity calculation of fully developed oscillating flow in a straight tube, it appeared that the stress-free boundary condition at the outlet gave rise to large oscillations in the velocities in the outstream region. Therefore, essential boundary conditions, describing fully developed oscillating flow in straight tubes, were applied to both ends of the curved tube for flow cases 5 and 6. To ensure that fluid flow was fully developed, the lengths of the instream and outstream sections for flow case 5 were chosen to be 20 times the radius of the tube. For flow case 6 the same element division was used as for flow case 1. Two-dimensional test calculations in straight tubes revealed that these lengths were reasonable estimates. Because of the long instream and outstream pipes for flow case 5 and owing to the limited capacity of the computer used for this calculation, the number of elements per cross-section had to be reduced to 20. The total number of elements in the axial direction was 28.

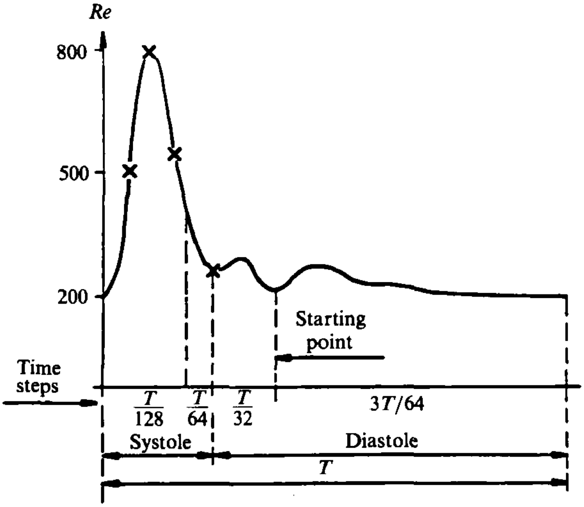

FIGURE 8. Timesteps and presentation levels for the physiological flow case.

In table 2 the number of periods needed to reach convergence are also presented. For flow cases 1, 2 and 3 the number of periods seems to be linearly dependent on the Womersley parameter. For these flow cases it was typical to see that the curvature of the axial isovelocity lines intensified with increasing period number. This phenomenon probably indicates that the number of periods needed to reach convergence is dominated by the development of the flow field induced by the steady flow component. For the physiological flow case one and a half periods were sufficient to reach convergence because flow at the end of the diastolic phase was found to be quasi-steady. For oscillating flow rates the number of periods appears to be smaller for higher Womersley parameters, which is different from the pulsatile flow cases. This is plausible owing to the absence of a steady flow component and the resulting lower secondary velocities at higher frequencies.

As for the reference case, the number of timesteps per period for flow cases 2, 3, 5 and 6 was 24. For the physiological flow case variable timesteps were applied, as pointed out in figure 8. The timesteps in the systolic phase were taken equal to $\frac{1}{128}T$, whereas the timesteps at the end of the diastolic phase were set equal to $\frac{3}{64}T$.

For flow cases 2, 3, 5 and 6 first an Euler-implicit time integration scheme was applied during $\frac{3}{4}T$, succeeded by a Crank–Nicolson scheme. For flow cases 2, 3 and 5, after 3 periods again an Euler-implicit time integration scheme was applied during $\frac{3}{4}T$ because of the bad convergence of the solution. All velocity calculations were started at minimal flow rate and used a zero velocity field as the initial condition. In the case of the physiological flow wave the calculation was started near the onset of the diastolic phase (figure 8). For this flow case during 11 timesteps an Euler-implicit time integration scheme was applied.

For all flow cases except 4, the results are presented at the same time levels as for the reference flow case, i.e. at mean flow rate in the acceleration phase ($t = 0$), at peak flow rate ($t = \frac{1}{4}T$), at mean flow rate in the deceleration phase ($t = \frac{1}{2}T$) and at minimal flow rate ($t = \frac{3}{4}T$). For the physiological flow wave the results are presented at the time intervals indicated in figure 8. At these time intervals the Reynolds numbers were equal to 500, 800, 540 and 265, respectively. To reduce the amount of data and because axial flow is a more or less prescribed quantity, only secondary velocity profiles are shown.

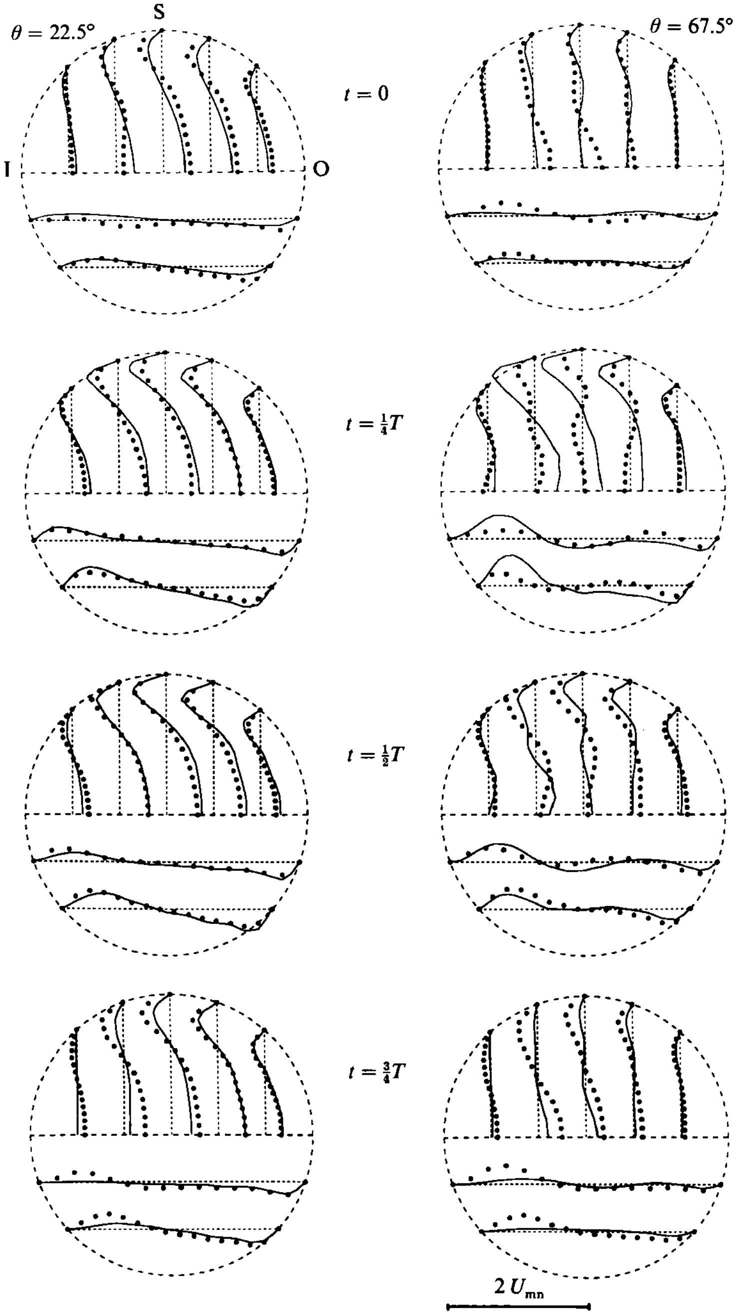

FIGURE 9. Secondary flow at $\theta = 22.5°$ and $67.5°$ for flow case 1 (—) and flow case 2 (⋯).

5.2. *Comparison between the various flow cases*

5.2.1. *The influence of the frequency parameter*

In figure 9 secondary flow at $\theta = 22.5°$ and $67.5°$ as a function of time is shown for flow cases 1 and 2 (flow case 2: $200 < Re < 800$, $\alpha = 15$, pulsating). At $\theta = 22.5°$ the secondary velocity profiles look the same for both flow cases. At minimal flow rate and halfway into the acceleration phase the secondary velocities are somewhat

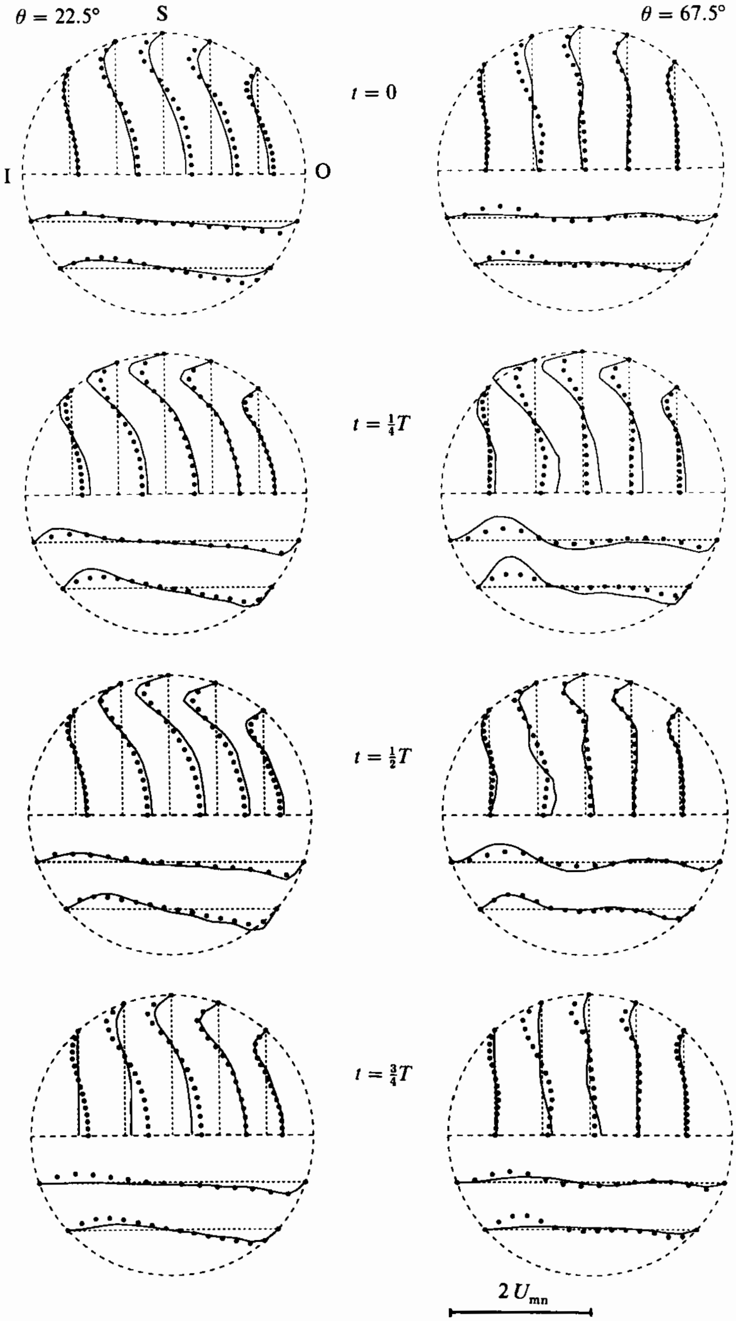

FIGURE 10. Secondary flow at $\theta = 22.5°$ and 67.5° for flow case 1 (—) and flow case 3 (····).

higher for flow case 2, whereas, at peak flow rate these velocities are somewhat lower. At $\theta = 67.5°$, however, secondary flow for flow case 2 shows complicated structures, especially at $t = \frac{1}{4}T$ and $\frac{1}{2}T$. At peak flow rate on each line both components of secondary flow are changing direction two or three times. Near the sidewall all secondary velocities are directed from the outer bend towards the inner bend. Near the plane of symmetry, however, secondary velocities are found directed from the

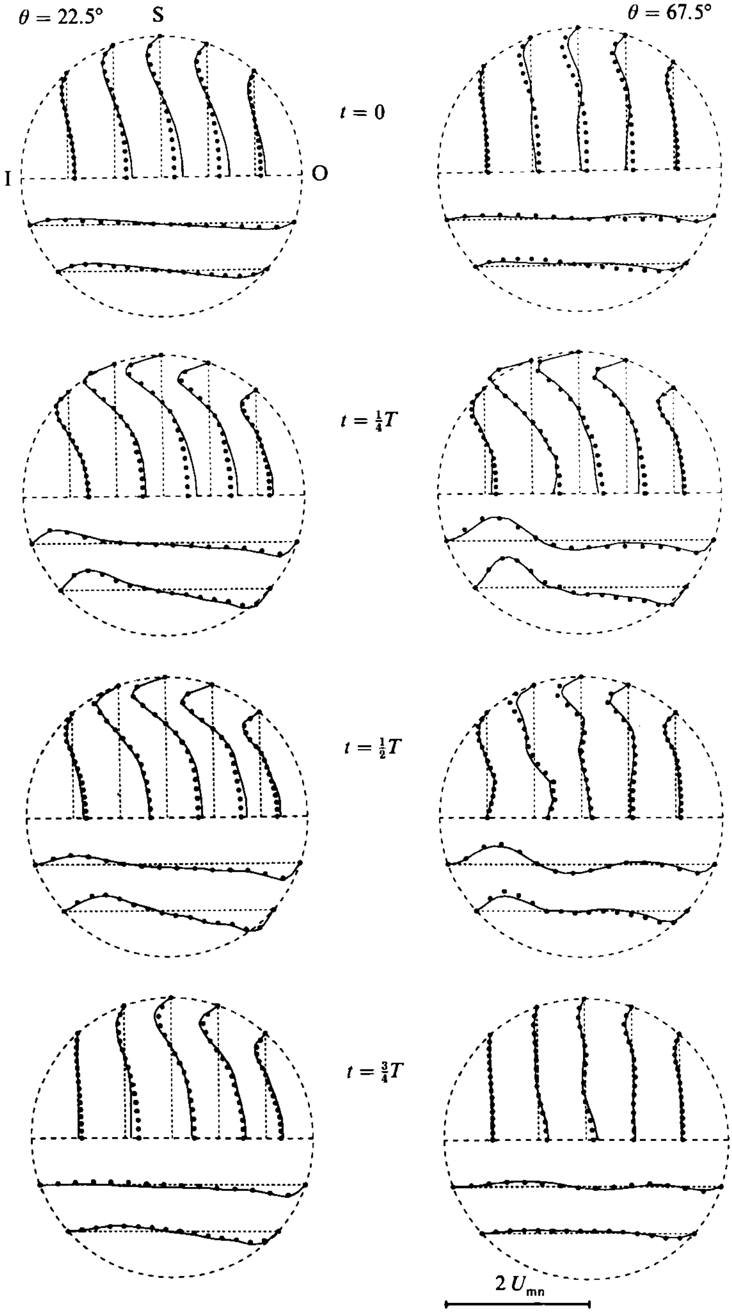

FIGURE 11. Secondary flow at $\theta = 22.5°$ and 67.5° flow case 1 (—) and flow case 4 (⋯).

inner bend towards the outer bend, as well as secondary velocities directed from the outer bend towards the inner bend, pointing to the development of Lyne-type structures. At all time intervals, except $t = \frac{1}{4}T$, the secondary velocities for flow case 2 are higher than the secondary velocities for the reference flow case.

In figure 10 the results are shown for flow cases 1 and 3 (flow case 3: $200 < Re < 800$, $\alpha = 24.7$, pulsating). At $\theta = 22.5°$ secondary flow has the same appearance as secondary flow for the reference flow case. The secondary velocities are somewhat higher for the time levels $t = 0$ and $\frac{3}{4}T$ and somewhat lower for $t = \frac{1}{4}T$ and $\frac{1}{2}T$. At $\theta = 67.5°$ larger differences are found in the secondary flow field. The irregular structures as found for flow case 2, however, are not present here. Throughout the flow cycle, the secondary velocities parallel to the plane of symmetry, are directed from the inner bend towards the outer bend near the plane of symmetry and circumferentially back near the sidewall. For flow case 3 at peak flow rate both secondary velocity components near the sidewall are lower, whereas these components are higher at minimal flow rate, as compared to the secondary velocities for the reference flow case. It is remarkable that the secondary velocity profiles for flow case 3 are almost constant in time at both positions. Apparently the unsteadiness of the flow rate at this high value of the Womersley parameter, hardly affects the secondary flow field.

5.2.2 *Influence of the flow wave form*

In figure 11 the results are shown for flow case 1 and flow case 4, the physiological flow wave (flow case 4: $200 < Re < 800$, $\alpha = 4$, physiological). From this figure it is observed that there is a rather fair agreement between the two flow cases with regard to secondary flow. The main differences are characterized by the somewhat higher secondary velocities for the physiological flow case at $t = 0$ and $\theta = 67.5°$. From this comparison it can be concluded that the influence of the diastolic phase on the flow phenomena occurring in the systolic phase is of minor importance.

5.2.3. *Influence of the steady flow component*

In figure 12 the secondary velocity profiles at $\theta = 45°$ as functions of time are presented for the oscillating flow cases. For $\alpha = 7.8$ the secondary flow field at $\theta = 45°$ resembles a pure Dean-type vortex at all time levels. These pure Dean-type vortices were also found at $\theta = 22.5°$ and $67.5°$ throughout the flow cycle. This is in contrast to the pulsating flow case where 'tail'-formation occurs further downstream in the curved tube at $\theta = 45°$, $67.5°$ and $90°$. Therefore, for these Reynolds numbers, it may be concluded that 'tail'-formation is a consequence of the steady flow component rather than of the unsteady one. The secondary flow field for $\alpha = 24.7$ shows a central core in which the velocities are directed towards the inner wall, whereas the Dean-type secondary vortex is situated near the sidewall. This points to a Lyne-type secondary flow field. The secondary velocities for $\alpha = 24.7$, however, are about 50 times lower than the secondary velocities for $\alpha = 7.8$. The oscillations in the numerical solution of the secondary flow field for $\alpha = 24.7$ are probably caused by a too coarse element division in radial direction.

6. Concluding discussion

6.1. *Summary of the results*

For steady entrance flow in a 90° curved tube ($Re = 700$, $\delta = \frac{1}{6}$) a shift of the maximum of axial velocity towards the outer wall occurs owing to centrifugal forces. The observed C-shaped axial isovelocity lines and the axial velocity plateaux near the inner bend, downstream in the curved tube, are caused by a Dean-type secondary flow field. Downstream in the curved tube 'tail'-formation (deflection of the Dean-type secondary vortex towards the sidewall) occurs in the secondary flow field, possibly caused by the fact that fluid particles with relative low axial and secondary

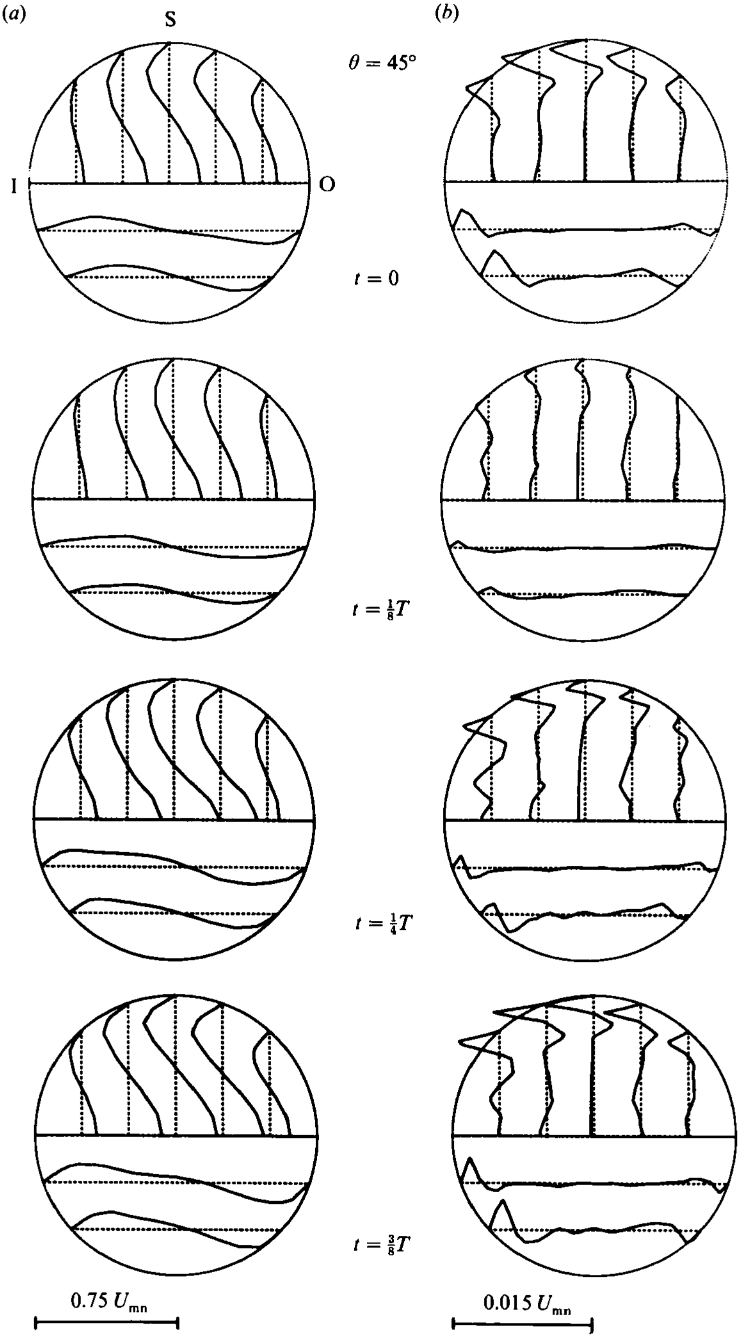

FIGURE 12. Secondary velocities halfway into the curved tube at $t = 0, \frac{1}{8}T, \frac{1}{4}T, \frac{3}{8}T$ for the oscillating flow cases 5(*a*) and 6(*b*). U_{mn} stands for the time-averaged mean axial velocity for the pulsating flow cases.

velocities near the centre of the tube are not able to penetrate into the region with high axial velocities near the outer wall.

For a fluid flow with a sinusoidally varying Reynolds number between 200 and 800 and a Womersley parameter of 7.8 (the reference flow case), great resemblance is found with the steady flow case halfway into the deceleration phase ($t = \frac{1}{2}T$). In contrast with the steady flow case, near the inner wall reversed axial flow regions are found halfway into the deceleration phase ($t = \frac{1}{2}T$) and at minimal flow rate ($t = \frac{3}{4}T$). Halfway into the curved tube, at $\theta = 45°$, a reversed axial flow region is also situated at the centre of the tube at minimal flow rate ($t = \frac{3}{4}T$). From $\theta = 45°$ towards $\theta = 90°$ the axial isovelocity lines show C-shaped contours at maximal flow rate ($t = \frac{1}{4}T$), which intensify in the deceleration phase. The secondary flow field is directed from the inner wall towards the outer wall near the plane of symmetry and circumferentially back near the sidewall of the curved tube, resembling a Dean-type secondary flow field. At all positions the highest secondary velocities occur at peak flow rate, but also halfway into the deceleration phase these velocities are high. As for steady flow, in the downstream end of the curved tube the secondary flow field shows 'tail'-formation in the deceleration phase, which is best visible at $t = \frac{1}{2}T$. At the entrance of the curved tube the secondary velocities are directed from the outer wall towards the inner wall, pointing at upstream influences of the tube.

The influence of an increase of the Womersley parameter is mainly observed in the secondary flow field. For $\alpha = 24.7$ the secondary flow field is almost constant in time at both positions $\theta = 22.5°$ and $67.5°$. A qualitative comparison of the secondary flow field with that found for the steady flow case at a Reynolds number of 700, reveals a good agreement. Therefore, it is presumed that secondary flow at higher frequencies is mainly determined by the steady flow component. A comparison of the secondary flow field for the physiological flow pulse ($\alpha = 4.0$) with the secondary flow field for the sinusoidally varying flow rate ($\alpha = 7.8$) reveals a good resemblance between the two flow cases. This supports the idea that the diastolic phase is only of minor importance for the systolic phase. Elimination of the steady flow component shows that for oscillating flow at $\alpha = 7.8$ the secondary flow fields at $\theta = 22.5°$, $45°$ and $67.5°$ are pure Dean-type vortices with a slightly varying vortex strength. No 'tail'-formation, as observed for the pulsating flow case, is present in the oscillating flow case suggesting that this 'tail'-formation is a consequence of the steady flow component rather than of the unsteady one. For oscillating flow at $\alpha = 24.7$ the secondary flow field shows a Lyne-type vortex at $\theta = 22.5°$, $45°$ and $67.5°$ and the secondary velocities are about 50 times lower than those for the pulsating flow case.

In general a comparison of the axial and secondary velocities determined by the numerical model with those obtained from laser-Doppler velocity measurements reveals a good agreement. The differences between the measured and calculated axial velocities are mainly caused by errors in the adjustment of the correct Reynolds number. The differences in the secondary velocities, however, have to be sought in the finite dimensions and positioning errors of the measuring volume, causing measuring problems near the sidewall of the curved tube. Besides, for the reference flow case numerical oscillations occur in the secondary flow field at the entrance of the curved tube. These oscillations are possibly caused by a too short inlet section or a too coarse element division in the axial direction. The observed oscillations in the numerical solution for the oscillating flow case at $\alpha = 24.7$ are probably caused by a too coarse element division in the axial and radial direction. Nevertheless, it may be concluded that the numerical model, as presented in this study, can be used to predict axial and secondary entrance flow in a 90° curved tube at moderate Reynolds numbers and Womersley parameters.

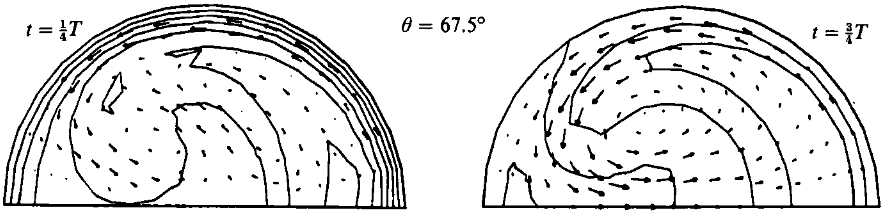

FIGURE 13. Axial and secondary flow for flow case 2 at $\theta = 67.5°$ and at $t = \frac{1}{4}T$ and $\frac{3}{4}T$.

6.2. *Comparison to literature*

A comparison of the results obtained in the present study with those reported in literature is difficult, because most studies deal with fully developed flows, which is probably only valid for the oscillating flow case at a Womersley parameter of 24.7. Studies dealing with unsteady entrance flow in curved tubes are mostly performed under totally different flow conditions. Nevertheless, a comparison is being made with the results of laser-Doppler velocity measurements performed by Talbot & Gong (1983). In their first experimental axial and secondary flow were measured in a 180° curved tube with a curvature ratio of $\frac{1}{20}$. The Dean number varied sinusoidally between 80 and 160 ($360 < Re < 720$) at a Womersley parameter of 8.0. At all positions and time intervals they observed a Dean-type secondary flow field. The plots of the profiles of the secondary velocity component parallel to the plane of symmetry do not suggest that 'tail'-formation occurred in the secondary flow field, as observed in the present study for the reference flow case (flow case 1: $200 < Re < 800$, $\alpha = 7.8$). At all time intervals the maximum of axial velocity shifted towards the outer wall. The C-shaped curvatures in the axial velocity contours, however, were only slightly in evidence or not present. In their second experiment fluid flow was investigated in a curved tube with a curvature ratio of $\frac{1}{7}$ for a sinusoidally varying flow rate at $\alpha = 12.5$ ($0 < \kappa < 744$; $0 < Re < 1970$). Especially at peak volume flow and halfway into the deceleration phase, complicated secondary flow fields were observed at $\theta = 60°$ and 110° with two regions where secondary flow was directed towards the outer wall and two regions where secondary flow was directed towards the inner wall. These secondary flow fields are quite similar to the secondary flow field which occurs in the present study for the pulsating flow case at $\alpha = 15$, $\theta = 67.5°$ and $t = \frac{1}{4}T$ (flow case 2: $200 < Re < 800$, $\alpha = 15$). In the second experiment of Talbot & Gong (1983) C-shaped axial velocity contours were observed downstream in the curved tube for all time intervals, except just before peak flow rate. The curvature of these C-shaped contours, however, was less pronounced as found in the present study (see figure 13). Finally, Talbot & Gong (1983) observed large regions with reversed axial flow near the inner bend. These regions are clearly due to the zero minimal flow rate.

Chang & Tarbell (1985) simulated the two experiments of Talbot & Gong (1983) numerically by a finite difference scheme based on the Navier–Stokes equations describing fully developed unsteady flow in curved tubes. As also observed for flow case 1 in their first experiment 'tail'-formation was found at the end of the deceleration phase. This 'tail'-formation, however, was absent at peak flow rate. Also the C-shaped axial velocity contours were less curved as observed for flow case 1. Probably, these differences are mainly caused by differences in the Dean number and the fact that Chang & Tarbell (1985) are dealing with fully developed flow. Comparison of the results for flow case 2 (figure 13) with the second experiment of

Chang & Tarbell (1985) reveals a rather good agreement at minimal flow rate (highly curved C-shaped axial velocity contours, reversal of axial flow near the inner wall, nearly 'tail'-formation in the secondary flow field), but a rather poor agreement at maximal flow rate. The results at maximal flow rate for flow case 2 seem to agree better with the results of Chang & Tarbell (1985) halfway into the deceleration phase (highly curved axial velocity contours, a complicated secondary flow field with several vortices). Probably the rather large difference in the Dean number contributes to this discrepancy.

Munson (1975) visualized for a range of Womersley parameters ($0.7 < \alpha < 32$) fully developed unsteady flow in a 360° curved tube with a curvature ratio $\delta = \frac{1}{14}$. In these experiments the secondary velocity component parallel to the plane of symmetry in the centre of the tube was measured as function of α. It was found that for values of α larger than 13 this secondary velocity component was directed towards the inner wall (Lyne-type secondary flow field), whereas for values of α smaller than 13 this secondary velocity component was directed towards the outer wall (Dean-type secondary flow field). The value of the outward directed component was large, as compared to the value of the inward directed component. Munson (1975) defined a time-averaged dimensionless quantity of this secondary velocity component, which was found to be 0.35×10^{-2} for $\alpha = 7.8$ and -0.15×10^{-3} for $\alpha = 24.7$. These values are 1.40×10^{-2} and -0.05×10^{-3}, respectively, at $\theta = 45°$ for the oscillating flow cases, as investigated in the present study. It is observed that the value of this quantity is indeed much smaller for $\alpha = 24.7$ than for $\alpha = 7.8$ and that opposite velocity directions are found. The relatively large difference with the value found by Munson (1975) for $\alpha = 7.8$ is probably caused by the fact that fluid flow at $\theta = 45°$ was not yet fully developed in our experiment. For both flow cases also the curvature ratio $\delta = \frac{1}{6}$ is relatively large compared to that of Munson (1975).

The authors are grateful to ir. F. C. M. van den Brand for his experimental assistance and to the National Fund for Supercomputers (NFS) for providing the supercomputer facilities.

REFERENCES

Berger, S. A., Talbot, L. & Yao, L. S. 1983 Flow in curved pipes. *Ann. Rev. Fluid Mech.* **15**, 461–512.

Bertelsen, A. F. 1975 An experimental investigation of low Reynolds number secondary streaming effects associated with an oscillating viscous flow in a curved pipe. *J. Fluid Mech.* **70**, 519–527.

Bovendeerd, P. H. M., Steenhoven, A. A. van, Vosse, F. N. van de & Vossers, G. 1987 Steady entry flow in a curved pipe. *J. Fluid Mech.* **177**, 233–246.

Chandran, K. B. & Yearwood, T. L. 1981 Experimental study of physiological pulsatile flow in a curved tube. *J. Fluid Mech.* **111**, 59–85.

Chandran, K. B., Yearwood, T. L. & Wieting, D. W. 1979 An experimental study of pulsatile flow in a curved tube. *J. Biomechanics* **12**, 793–805.

Chang, L. J. & Tarbell, J. M. 1985 Numerical simulation of fully developed sinusoidal and pulsatile (physiological) flow in curved tubes. *J. Fluid Mech.* **161**, 175–198.

Crouzeix, M. & Raviart, P. A. 1973 Conforming and nonconforming finite element methods for solving the stationary Stokes equations. *RAIRO Anal. Num.* R3, 33–76.

Cuvelier, C., Segal, A. & Steenhoven, A. A. van 1986 *Finite Element Methods and Navier–Stokes Equations*. Dordrecht: D. Reidel.

Dean, W. R. 1972 Note on the motion of fluid in a curved pipe. *Phil. Mag.* **4**, 208–223.

Drain, L. E. 1981 *The Laser Doppler Technique*. John Wiley & Sons.

HAMAKIOTES, C. C. & BERGER, S. A. 1988 Fully developed pulsatile flow in a curved pipe. *J. Fluid Mech.* **195**, 23–55.

LIN, J. Y. & TARBELL, J. M. 1980 An experimental and numerical study of periodic flow in a curved tube. *J. Fluid Mech.* **100**, 623–638.

LYNE, W. H. 1970 Unsteady viscous flow in a curved pipe. *J. Fluid Mech.* **45**, 13–31.

MULLIN, T. & GREATED, C. A. 1980 Oscillatory flow in curved pipes. Part 1. The developing-flow case; Part 2. The fully developed case. *J. Fluid Mech.* **98**, 383–416.

MUNSON, B. R. 1975 Experimental results for oscillating flow in a curved pipe. *Phys. Fluids* **18**, 1607–1609.

OLSON, D. E. 1971 Fluid mechanics relevant to respiration: flow within curved or elliptical tubes and bifurcating systems. PhD thesis, University of London.

PELISSIER, M. 1975 Resolution numérique de quelques problèmes raides en mecanique des milieux faiblement compressibles. *Estratto da Calcolo* **12**, 275–314.

PERKTOLD, K., FLORIAN, H. & HILBERT, D. 1987 Analysis of pulsatile blood flow: a carotid siphon model. *J. Biomed. Engng* **9**, 46–53.

RINDT, C. C. M., VOSSE, F. N. VAN DE, STEENHOVEN, A. A. VAN, JANSSEN, J. D. & RENEMAN, R. S. 1987 A numerical and experimental analysis of the flow field in a two-dimensional model of the human carotid artery bifurcation. *J. Biomech.* **20**, 499–509.

SEGAL, A. 1984 *Sepran User Manual and Programmers Guide.* Ingenieurs buro Sepra, Leidschendam.

SINGH, M. P., SINHA, P. C. & AGGARWAL, M. 1978 Flow in the entrance of the aorta. *J. Fluid Mech.* **87**, 97–120.

SLOAN, S. W. 1986 An algorithm for profile and wavefront reduction of sparse matrices. *Intl J. Numer. Meth. Engng* **23**, 239–251.

SMITH, F. T. 1975 Pulsatile flow in curved pipes. *J. Fluid Mech.* **71**, 15–42.

TALBOT, L. & GONG, K. O. 1983 Pulsatile entrance flow in a curved pipe. *J. Fluid Mech.* **127**, 1–25.

TEMAM, R. 1977 *Navier–Stokes Equations, Theory and Numerical Analysis*, 2nd edn. North Holland.

VOSSE, F. N. VAN DE, SEGAL, A., STEENHOVEN, A. A. VAN & JANSSEN, J. D. 1986 A finite element approximation of the unsteady 2D–Navier–Stokes equations. *Intl. J. Numer. Meth. Fluids* **6**, 427–443.

VOSSE, F. N. VAN DEN, STEENHOVEN, A. A. VAN SEGEL, A. & JANSSEN, J. D. 1989 A finite element analysis of the steady laminar entrance flow in a 90° curved tube. *Intl. J. Numer. Meth. Fluids* **9**, 275–287.

ZALOSH, R. G. & NELSON, W. G. 1973 Pulsating flow in a curved tube. *J. Fluid Mech.* **59**, 693–705.